Fatigue failure mechanisms for AlSi10Mg manufactured by L-PBF under axial and torsional loads: the role of defects and residual stresses

F. Sausto[a], P. E. Carrion[b,c], N. Shamsaei[b,c], S. Beretta[a,*]

[a]*Department of Mechanical Engineering, Politecnico di Milano, via La Masa 1, 20156, Milano, Italy*
[b]*Department of Mechanical Engineering, Auburn University, Auburn, AL 36849, USA*
[c]*National Center for Additive Manufacturing Excellence (NCAME), Auburn University, Auburn, AL 36849, USA*

Abstract

Additive Manufacturing (AM) is with no doubt the most revolutionary manufacturing process developed in the last two decades. Despite the indisputable advantages of this technology, the poor surface quality of net-shape components, the presence of internal defects and the development of process induced residual stresses still represent the main problems for the fatigue strength of critical stressed components. In previous works investigating the same alloy, the uniaxial fatigue strength of both machined and net-shape specimens was correlated with the defect size through a Kitagawa diagram, allowing to describe the problem from the threshold perspective. The aim of this work is to extend this approach by investigating the failure mechanisms under torsion in presence of manufacturing defects, both volumetric and superficial anomalies. Specimens manufactured with laser powder bed fusion (L-PBF) technique out of AlSi10Mg, featuring both machined and net-shape surface state, were tested and analysed. The two experimental campaigns allow to investigate the competition between internal defects and superficial features and their effect on the fatigue performances. Tests were performed under two loading conditions, namely fully reverse torsion ($R_T = -1$) and positive torque ratio ($R_T = 0.1$). It was found that for the net-shape specimens manufacturing residual stresses have a key role in influencing fatigue strength of this material, making the fatigue limit in torsion of the two considered loading conditions comparable. All the tested specimens failed onto a maximum principal stress plane, which is in line with multiaxial tests performed on a cast A356-T6 aluminium alloy. In some relatively high shear stresses there is a competition between Mode I and Mode II crack propagation, whose threshold condition is controlled by $\Delta K_{\mathrm{th,I}}$.

Keywords: Additive manufacturing, AlSi10Mg, torsional fatigue, net-shape components.

*Corresponding author
Email address: stefano.beretta@polimi.it (S. Beretta)

Nomenclature

a crack depth

A, B parameters of the S-N curve

A_t strain at rupture

c length of the elliptical crack

E Young's modulus

E_stab stabilized cyclic Young's modulus

F_LEVD cumulative density function of the largest extreme values distribution

K_{II} Mode II stress intensity factor

K_t stress concentration factor

N_f number of cycles to failure

N_k knee point of the S-N curve

R_a arithmetic mean of the deviation of the profile over the evaluation length

R_c mean height of the profile elements

R_eff effective stress range

R_L axial load ratio

R_p maximum profile peak height

$R_\mathrm{p0.2\%}$ 0.2 % of the plastic tensile stress

R_sm mean width of profile elements

R_T torque load ratio

R_t maximum profile height

R_v maximum profile valley depth

t depth of the superficial feature

w total length of the superficial feature

Y Murakami's boundary correction factor

δ scale parameter of the LEVD

λ location parameter of the LEVD

$\sigma_{\log S}$ standard deviation of the fatigue limit

$\sigma_{\log N}$ standard deviation of the S-N curve in terms of number of cycles to failure

$\sigma_\mathrm{max}^\mathrm{eff}$, $\sigma_\mathrm{min}^\mathrm{eff}$ maximum and minimum effective stress

σ_RS residual stress

σ_Y material yield stress

$\Delta K_\mathrm{th,I}$ Mode I crack threshold

$\Delta K_\mathrm{I,tens}$ SIF range for Mode I cracks loaded in tension

$\Delta K_\mathrm{I,shear}$ SIF range for Mode I cracks loaded in shear

ΔK_{II} SIF range for Mode III cracks

Δk_I local SIF range in Mode I at the twist plane

$\Delta K_\mathrm{th,lc}$ SIF range threshold for long cracks

$\Delta \sigma_\mathrm{w0}$ fatigue stress range limit for defect-free material

$\Delta \sigma$ stress range

$\Delta \tau$ shear range

$\Delta \sigma_\mathrm{w}$ fatigue stress range limit

$\Delta \tau_\mathrm{w}$ fatigue shear range limit

$\Delta \mathrm{S}_\mathrm{lim}$ general fatigue limit

Φ angle between the main specimen's axis and the residual stress measuring direction

$\sqrt{\mathrm{area}}$ square root of the defect area

$\sqrt{\mathrm{area}}_\mathrm{p}$ square root area projected on the maximum principal stress plane ($\sqrt{\mathrm{area}}_\mathrm{p} = \sqrt{\mathrm{area}} \cdot \cos(\pi/4)$)

$\sqrt{\mathrm{area}}_0$ El-Haddad parameter

Abbreviations

AM	additive manufacturing
AMed	additive manufactured
FWHM	full with at half maximum
HCF	high cycle fatigue
HIP	hot isostatic pressuring
LEFM	linear elastic fracture mechanics
LEVD	largest extreme values distribution
LoF	lack of fusion
L-PBF	laser powder bed fusion
SEM	scanning electron microscope/microscopy
SIF	stress intensity factor
S-N	stress range over number of cycles to failure
SPP	spherical powder particles
UTS	ultimate tensile stress
XRD	X-ray diffraction measurements method

1. Introduction

The scientific interest about Additive Manufacturing (AM) technology has been growing more and more in the last two decades, both for the manufacturing and its application for fatigue critical components. Despite the unquestionable advantages of AM, the alloys produced with this technology are still affected by a series of drawbacks that limit them applications to load-bearing components [1]. Unavoidable drawbacks related to this manufacturing process are the presence of internal defects, poor surface quality and residual tensile stresses [2, 3].

It is consolidated in technical literature that internal defects, like lack of fusions (LoFs), pores and spatters, play a key role in the high scatter of the fatigue results especially in high cycle fatigue conditions (HCF) [4, 5, 6, 7]. To reduce the fatigue scatter, a defect tolerant approach is then required, in particular the adoption of the Murakami $\sqrt{\text{area}}$ approach [8] was shown to correlate well with the experimental results of AM materials in terms of fatigue strength [5], finite stress life [9] and finite strain life [10, 11]. Usually load-bearing components show a fatigue strength much lower than the laboratory specimens. From a probabilistic point of view the probability to find a big defect inside the material increases with the increasing of the volume, this is also known as *scaling effect* [12]. Considering suitable statistical models for defect sizes [12, 13] and the Kitagawa-Takahashi diagram, it is possible to estimate fatigue performances at level of specimens [5, 13, 14] or components [15].

The main advantage of AM is the possibility to obtain complex geometries, that could be very difficult from conventional processes. There is hence a stringent requirement to understand the fatigue properties of the AM *net-shape* surfaces. The layer-by-layer nature of the AM building process produces parts with a poor surface roughness [16], which is influenced by the presence of partially un-melted particles, spatters and balling [17]. All these features directly influence the fatigue strength of the net-shape material, that can be considered as micro-notches on the surface and hence preferential locations for fatigue cracks nucleation [18, 19, 20, 21, 22, 23]. Beretta et al. [24] and Romano et al. [25] demonstrated that the same $\sqrt{\text{area}}$ approach used for internal defects, can be transferred to the rough surfaces with acceptable match with the experimental results, obtained for AMed AlSi10Mg and 17-4 PH stainless steel, respectively. However, the description of rough surface features from a statistical point of view is still a debatable point [12].

Although the internal defects and superficial features are found to directly influence the fatigue of AMed parts, the presence of manufacturing residual stresses, especially when in tension, cannot be neglected during the components' design phase. As happens for the conventional welding process [26], the effect of consecutively remelting by the laser track can introduce tensile residual stresses in the AMed materials [27, 28]. In general the residual stresses are influenced by several parameters like the orientation of the produced part, position of the supports and manufacturing parameters [29, 30]. The presence of residual stresses increases the complexity of studying the fatigue properties of AMed materials by both influencing the effective stress ratio at which the components are subjected during the loading [24], and introducing a multiaxial state of stress even if in presence of uniaxial external forces [31].

Considering all the features related to AMed materials, it seems necessary to study the fatigue problem from a multiaxial point of view, taking into account the effects of both internal defects and superficial features. One of the first study about the multiaxial fatigue of AMed material was conducted by Fatemi et al. [32] on a Ti6Al4V alloy. In this study, the multiaxial fatigue of wrought Ti6Al4V material was compared with that of the AMed version in both machined and net-shape superficial conditions. Wrought material was found to fail in shear mode for both the multiaxial loading conditions. Irrespective of the surface state, all printed specimens were found to fail along the maximum principal plane. The multiaxial fatigue life was found to be lower for the AMed material respect to that wrought; this was justified with the presence of internal defects for the machined specimens and of superficial features for the net-shape ones.

The same alloy was then used to evaluate the pure torsional fatigue behaviour between wrought and AMed material in [33]. The failures due to torsional loads were along the maximum shear plane for wrought material, and along the maximum principal stress plane for the AMed specimens at the fatigue limit. Machined torsional specimens were found to have higher fatigue properties with respect to those net-shape, but still inferior to the wrought counterparts.

Molaei et al. [34] repeated the same multiaxial tests of Fatemi et al. [32] considering the same Ti6Al4V alloy printed with the same machine (Reinshaw AM250) and with another one (EOS M290). Both machined and net-shape specimens were HIPed before the testing. It was found that the HIP process was able to reduce the dimension of internal defects of both batches. The reduction of internal defects was beneficial for the fatigue life, with experimental points almost reaching those obtained for the wrought material. The reduced dimension of internal defects was also able to shift the failure mechanism from tensile to shear at the fatigue limit. The net-shape specimens show no increment in terms of fatigue performance after the HIP, with a tensile failure mechanism at the fatigue limit [35]. To take into account both the dimension of defects and the failure mechanisms, Sanaei [9] analysed the experimental results in [32, 34] considering a fracture mechanics approach based on the Hartman-Schijve variation of the NASGRO equation. The numerical estimations were found to fit reasonably well with the experimental evidences.

To the authors' best knowledge, no multiaxial tests are available in literature performed on AlSi10Mg alloy produced by AM. Several torsional and multiaxial tests are instead reported in the open literature about the cast aluminium. Le et al. [36] performed a series of multiaxial tests on a AlSi alloy obtained by three different casting methods. Each of the three batches was featured with a different mean defect size. It was found that defects bigger than the average grains size failed on tensile mode, while those smaller on shear. These results and the ones obtained by the research group of Fatemi [32, 34, 35] seem to suggest a relation between the failure mechanism and the dimension of the killer defect.

A recent work by Avval et al. [37] shows the results of multiaxial tests performed on casting A356-T6 aluminium alloy specimens. All the failures happen on the maximum principal stress plane. In both the works by Le [36] and Avval [37] the microstructure of the alloys is the main driver of the failure mechanisms. This is because the dimension of the found defects is big enough to guarantee that the failure strength is

always controlled by the linear elastic fracture mechanics (LEFM), lowering the stress range at which the material is cycling [38]. Taking into account this evidence, the authors used a fatigue model based on the maximum principal alternate stress to explain the experimental results, with a good match.

1.1. Aim of the work

The aim of this research is to study the torsional fatigue performance of the AlSi10Mg, considering both machined and net-shape surface conditions. The obtained results are then compared with those coming from uniaxial fatigue tests. This alloy was the same analysed by Beretta et al. [24] and Du Plessis et al. [39].

Several works dealing with the relation between the fatigue strength in torsion and cracks emanating from spherical [40, 41, 42] and semi-elliptical defects [43, 44, 45] are reported in the open literature. The idea behind this work is to adapt these state-of-art models to correlate the torsional fatigue of AlSi10Mg with the dimension of internal defect and superficial features in a Kitagawa-Takahashi diagram. According to the results available in literature, the fatigue limit in torsion is in general lower that that in tension/bending [40], due to the more detrimental state of stress at which a crack is subjected. According to this evidence, it is expected the material to behave as that represented in Figure 1.a, with the machined material fatigue limit higher than that for the net-shape due to the different defects size.

The effect of different load ratios on the fatigue performances is considered too, performing the tests at two different torsional ratios ($R_T = -1$ and $R_T = 0.1$). The fatigue strength of both machined and net-shape specimens is expected to be influenced by the presence of manufacturing defects and they will depend on stress ratio, being controlled by fracture mechanics models in which the stress ratio influences the crack's threshold ΔK_{th} for both short and long cracks. In absence of defects the torsional fatigue limit of the material does not change with the applied stress ratio [46, 47]. This is schematically reported in Figure 1.b, in particular it is expected a torsional fatigue limit for the machined specimens higher than the one for the net-shape specimens for both load ratios (defects for machined ones expected to be smaller than the net-shape ones).

The paper is organized as follows: in Section 2 the printing parameters as well as the experimental set-ups are presented and described; Section 3 aims to present all the experimental results related to fatigue tests, fracture surface analysis with scanning electron microscope (SEM) and residual stresses measurements; in Section 4 the results are discussed and the models used to describe them are presented; Section 5 aims to the adoption of the defect sensitive fatigue models and the comparison with the experimental data sets; and conclusions are then drawn in Section 6.
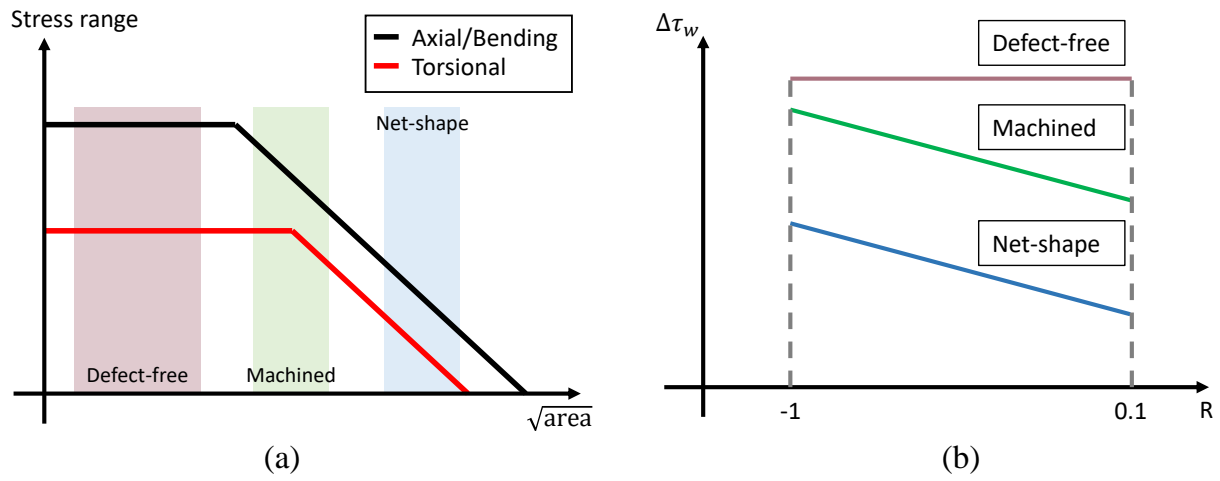
Figure 1: Expected results: a) comparison between the defect distributions of defect-free, machined and net-shape materials plotted in the Kitagawa diagram and b) reduction of shear fatigue limit due to the applied load ratio.

2. Material and experiments

Fatigue specimens used in this study were fabricated by a laser powder bed fusion (L-PBF) technique, before testing all the specimens were heat treated with a T5 thermal treatment. Specimens were fabricated in *net-shape* and with an oversized gauge section to allow further machining. An overstock of 0.2 mm of material was considered in the zones that needed a mechanical machining before testing. All the specimens in this work were printed vertically and asymmetrically respect to the gauge section, with a lower part 30 mm longer than that upper to allow the machining by lathe as shown schematically in Figure 2.a.

The specimens were manufactured using an SLM 280HL v1.0 system equipped with 2×400 W Yttrium fibre lasers that work in parallel in a build chamber of $280 \times 280 \times 350$ mm^3 (SLM Solution Group AG). During the manufacturing process, the chamber was flooded with argon to reduce the oxygen content to below 0.2 %. The printing parameters were set as: laser power of 350 W, hatch distance of 0.13 mm and scan speed of 1650 mm s^{-1}. A layer thickness of 50 µm was used resulting in an energy density of 32.63 J mm^{-3}; the building platform was heated up to 150 °C. The scan strategy is stripes which rotates each layer by 67° and the scanning order is two contours followed by the hatch scanning. AlSi10Mg powder was produced by ECKA granules, which feature a mean size of 37 µm, D10 of 21 µm and D90 of 65 µm with a flowability of 80 s/50 g.

The gauge sections of the specimens were the same for both machined and net-shape surface conditions. Machined specimens were printed considering a material overlayer onto both gauge and gripping zones, while those net-shape for axial tests were printed considering the nominal gauge dimensions with a material overstock onto only the gripping sections. Torsional net-shape specimens were as well printed with the nominal dimensions of the gauge section, with a cylindrically shaped gripping zones of 18 mm diameter. The gripping zones were then milled to obtain a squared section, as required by the torsional resonant machine. The main dimensions with the gauge surface state of the specimens are reported in Figure 2.b to Figure 2.d. The test plan with a detailed indication of the machines utilized and the number of specimens tested is reported in Table 1.

The roughness of the net-shape specimens was evaluated with an optical microscope Keyence VHX-6000X, considering a surface of 3 mm × 1 mm. The analysed surface was obtained by the stitching of a series of acquisitions by using a magnification of 500x, following the findings by Lee et al. in [48]. The roughness parameters were computed onto five equispaced lines of 3 mm. The standards roughness parameters R_a (arithmetic mean roughness), R_p (maximum profile peak height), R_z (maximum height), R_v (maximum profile valley depth), R_v (maximum profile valley depth) and R_t (total height) were computed as prescribed by the standards ISO 4287 [49] and ISO 4288 [50]. The roughness parameters R_c (mean height of the profile elements) and R_{sm} (mean width of profile elements) were computed as well, with the algorithms proposed by Seewing et al. [51]. The obtained results are summarized in Table 2 for all the analysed profiles.

Two machined and net-shape specimens were cut longitudinally and transversally respect to the main specimen axis. The obtained portions were cold mounted in epoxy resin, mirror polished and chemical etched

with the Keller's reagent (95 mL water, 2.5 mL HNO3, 1.5 mL HCl, 1.0 mL HF) for 20 s. The etched sections were observed by means of an optical microscope, the results with a schematic of the observed directions respect to the cut portions of the samples are shown in Figure 3. The analysis showed the typical geometry of the melting pool due to the laser scanning featured with some pores, which is line with the results showed by Romano et al. [10] for the same alloy. As can be noted the machining does not evidently influence the microstructure. However, the typical rough layer of net-shape specimens is completely removed, i.e. the contour layer, evident in Figure 3.f and Figure 3.h. It has been shown that the main part of defects is concentrated near the external surface [3, 25], therefore the elimination of the external material layer influences the volumetric defects population.
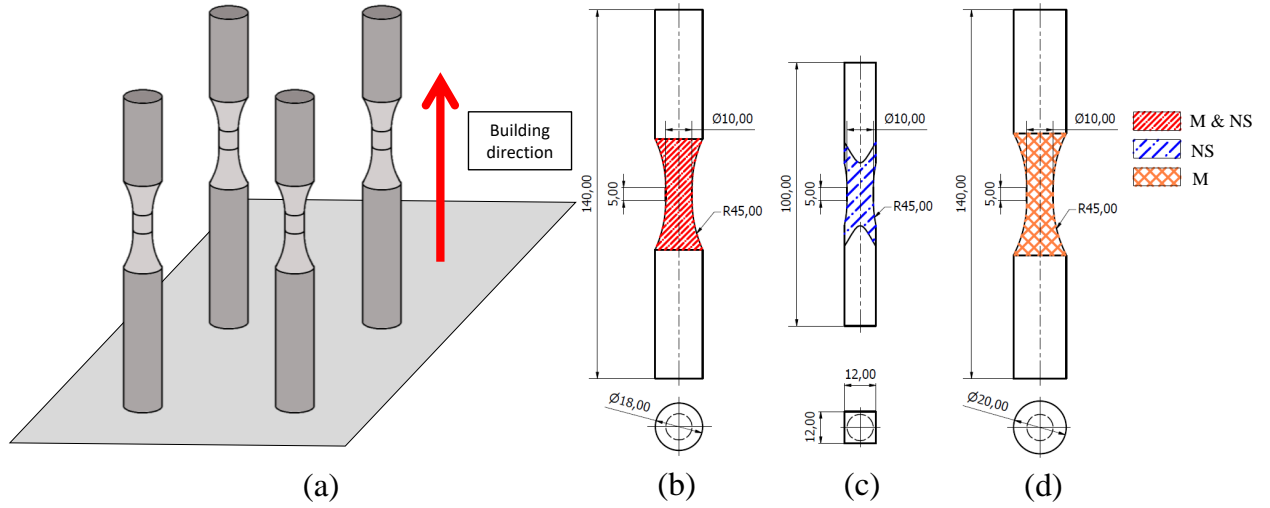

Figure 2: Fabricated specimens of the experimental campaign: a) scheme of the printed specimens respect to the building plate; b) main dimensions of the axial specimens for servo-hydraulic testing machine; c) main dimensions of the torsional specimens for resonant testing machine; d) main dimensions of the torsional specimens for servo-hydraulic testing machine. The dimensions of the specimens were in accordance with the standard BS ISO 1352 [52].

Table 1: Summary of the tests performed on both machined and net-shape specimens.

Nomenclature	Loading path	Surface state	Stress ratio	Machine	Number of tests
Series B	Axial	Machined	-1	Servo-hydraulic	11
Series G	Axial	Net-shape	-1	Servo-hydraulic	14
Series D	Torsional	Machined	-1	Servo-hydraulic	11
Series C	Torsional	Machined	0.1	Servo-hydraulic	10
Series E	Torsional	Net-shape	-1	Resonant	15
Series F	Torsional	Net-shape	0.1	Resonant	11

Table 2: Surface roughness of net-shape specimen are measured according to ISO 4287 [49], ISO 4288 [50] and the reviewed parameters R_c and R_{sm} by Seewig et al. [51].

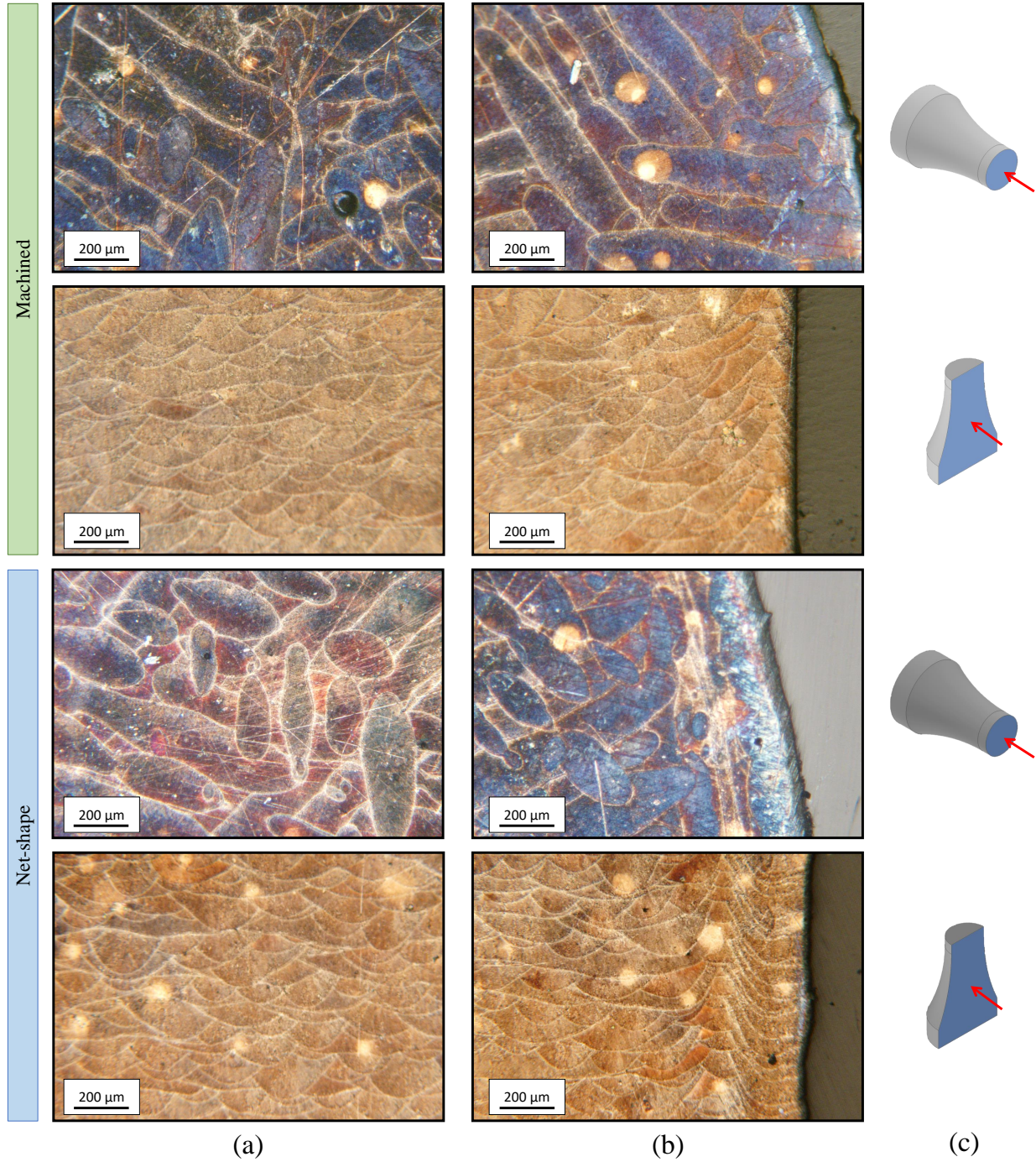| Parameters [µm]	Profile 1	Profile 2	Profile 3	Profile 4	Profile 5	Representative results
R_a	8.12	5.71	6.31	8.03	5.93	6.82 (mean)
Rp	38.37	17.37	19.96	31.09	37.07	38.37 (maximum)
R_v	19.77	23.58	16.27	21.85	18.35	23.58 (maximum)
R_t	58.14	40.95	36.23	52.94	55.41	58.14 (maximum)
R_c	27.27	18.21	21.71	19.21	20.94	21.47 (mean)
R_{sm}	280.42	364.51	253.98	210.28	242.04	270.25 (mean)

Figure 3: Optical microscopy of the AlSi10Mg after the chemical etching: a) observation of the bulk material; b) observation of the contouring region and c) schematic of the transverse and longitudinal observation of the samples.

2.1. Axial fatigue tests

The specimens used to characterize the uniaxial fatigue properties of the AlSi10Mg alloy considered in this work are shown with the main dimensions in Figure 2.b. To minimize the geometrical effect on the fatigue results, they were manufactured with the dimensions suggested by BS ISO 1352 [52] standard. The results of these tests have to be considered as a reference for those torsional, being not conformed to any uniaxial fatigue standard available in the technical literature. Tested specimens were featured with both machined and net-shape surface state of the gauge section. Machined specimens were obtained by mechanical removal of the overlayer material by lathe; the parallel section of the specimens was mechanically polished by emery paper with a mesh size of 250 to 2500, in order to remove the deep machining marks. The net-shape specimens were printed considering the gauge section with the nominal dimensions shown in Figure 2.b, while the gripping sections featured a 0.2 mm of overstock material. This was then mechanically removed in order to reach a sufficient axial accuracy to perform the fatigue tests.

The fatigue tests were conducted under a force control logic on a servo-hydraulic MTS Landmark testing machine with a maximum force capacity of 100 kN. Tests ended with the complete fracture of the specimens. All the tests were performed imposing a global load ratio of $R_L = -1.0$, with a frequency of 25 Hz. Tests that reached 5×10^6 cycles without fracture were considered as *Run-Outs*, those specimens were retested at higher stress range in order to reach the fatigue rupture and measure the manufacturing defect. After the fatigue rupture, the distance between the mean height of the gauge length and the crack initiation site was measured; by using this quantity and the normalized stress distribution along the specimen surface in the axial direction, obtained with a FE analysis, the effective stress range for the failure section was then computed. From now on the axial machined specimens will be referred to as *Series B*, while those net-shape as *Series G*.

2.2. Torsional fatigue tests

The dimensions of the specimens used for the HCF torsional tests are reported in Figure 2.c and Figure 2.d, which are in line with those suggested in BS ISO 1352 [52] standard. Both machined and net-shape surface states of the gauge section were considered in this experimental campaign.

The geometry of the net-shape specimens is that shown in Figure 2.c. These specimens were printed as bars, with the same dimensions of the gauge central section reported in Figure 2.c and a diameter of 18 mm for the gripping zones. The specimens were printed asymmetrically with respect to the gauge section, with the lower part 30 mm longer than the upper part. This was chosen to help with the machining of the gripping sections, which were milled to obtain a squared section. After the cutting of the exceeding material of the lower part, no further machining was performed. Tests were performed on a torsional resonant RUMUL machine equipped with a 160 N m load cell with a mean frequency of 60 Hz. Tests were performed considering a global torque ratio of $R_T = -1$ and $R_T = 0.1$. A frequency drop of 3 Hz was considered as a failure condition for the specimens.

Dimensions of the machined specimens were reported in Figure 2.d. These specimens were printed considering a material overstock of 0.2 mm in both gauge and gripping sections; these were then mechanically removed to reach the nominal dimensions in Figure 2.d. Before testing, the gauge section was polished by emery paper with a mesh size of 250 to 2500 in order to remove the deep machining marks. The tests were performed on a servo-hydraulic MTS 809 axial/torsion testing machine with a maximum torque of 1100 N m. Tests were performed considering a global torque ratio of $R_T = -1$ and $R_T = 0.1$. A specimen was considered broken if the torsional angle during the test overcome an increment of 10 % with respect to the initial condition.

Tests that reached 5×10^6 cycles without fracture were considered as *Run-Outs*, those specimens were retested at higher shear stress range in order to reach the fatigue rupture and measure the killer manufacturing defect. Specimens were statically broken after the application of a torque, which direction was chosen to keep the crack open during the fracture. The relative distance between the crack initiation plane and those at the mid gauge section was measured in order to calculate the real shear stress range which causes the failure of the specimen.

2.3. Residual stress measurements

Manufacturing residual stresses were measured on both machined and net-shape specimens with an AST X-Stress 3000 portable X-ray diffractometer (CrKα radiation), using a $\sin \psi^2$ method with a diffraction angle $2\theta = 139°$. Three measurements were performed on the net-shape torsional specimens, namely longitudinal ($\Phi = 0°$), transversal ($\Phi = 90°$) and diagonal ($\Phi = 45°$). With these three measurements it was then possible to find the orientation of the principal reference system of the residual stresses, that corresponds to the printing one. Measures were performed on two opposite faces of the specimens at four different depths, namely 0 µm (superficial), 50 µm, 100 µm, and 500 µm. Material erosion was performed by electro-polishing of a circular area of 5 mm diameter in the central zone of the specimens' gauge section. The electrolytic solution adopted was composed by 94 % of acetic acid (CH3COOH) and 6 % perchloric acid (HClO4), with a voltage of 45 V and a current between 0.55 A and 0.65 A. After each electro-polishing step, a Mitutoyo micrometre was used to evaluate the effective erosion depth.

Residual stress measurements of the axial machined and net-shape specimens were performed only on longitudinal and transversal directions, $\Phi = 0°$ and $\Phi = 90°$ respectively. Three measurements on the specimens' surface were performed, spaced 120° each. Measures were repeated at three depths as done for the torsional specimens, at 0 µm (superficial), 50 µm and 100 µm. To compare the results with the torsional specimens, the residual stresses were measured on one net-shape specimen at five depths, namely 0 µm (superficial), 50 µm, 100 µm, 300 µm and 500 µm.

2.4. Fracture analysis

After the final rupture of the axial fatigue tests, fracture surfaces were cleaned under an ultrasonic action in ethanol to eliminate any dirt or dust. A global analysis of the fracture surfaces was firstly performed with

13

a stereo microscope, then a more accurate analysis was performed with an SEM EVO 50 manufactured by Zeiss.

Torsional tests were performed with resonant testing machines, that are able to stop the test before the final rupture. Cracked specimens were broken by means of servo-hydraulic testing machine by firstly apply a slight torsion in order to keep the crack open, followed by an axial load causing the final fracture of the specimen. A global analysis of both the crack path and the fracture surface were performed on a stereo microscope. Then a more accurate analysis was performed under the SEM, observing the defects at the crack initiation sites.

3. Results

3.1. Tensile and cyclic properties

Seven tensile cylindrical specimens were printed and machined, featured with a gauge diameter of 6 mm and 36 mm long parallel section as prescribed by the standard BS ISO 6892 [53]. The obtained mean tensile properties are collected in Table 3.

Table 3: Mean tensile properties of the AlSi10Mg considered in this work.

E [GPa]	$R_{p0.2\%}$ [MPa]	UTS [MPa]	A_t [%]
72.5	212.2	381.5	5.7

Three of the printed specimens were adopted for a strain controlled test with the aim of obtaining the cyclic properties of the material. These were machined to obtain a cylindrical specimen with a gauge diameter of 8 mm and 20 mm long, following the prescriptions of ASTM standard E606 [54]. The strain amplitude was applied incrementally in five successive blocks of 0.2 %, 0.4 %, 0.5 %, 0.6 % and 0.7 % respectively. A stabilized cyclic Ramberg-Osgood curve was therefore fitted with the experimental data-points, which parameters are reported in Table 4

Table 4: Parameters of the cyclic curve of AlSi10Mg considered in this work.

E_{stab} [GPa]	K' [MPa]	n' [-]
73.7	852.5	0.2218

3.2. SN curves

The results of the axial and torsional HCF tests are presented in Figure 4.a and Figure 4.b, respectively for machined and net-shape specimens; the right-pointing triangles are the *Run-Outs*. Axial fatigue data-points are represented with hollow symbols, while those solid indicate the torsional tests. Experimental data-points in the finite life regime were fitted with a three parameters Gaussian distribution, with the mean value described by Equation (1) and considering a constant standard deviation $\sigma_{\log N}$, as prescribed by ASTM

E739 [55]:

$$N_f = A \cdot \Delta\sigma^B \tag{1}$$

where N_f is the number of cycles to failure, $\Delta\sigma$ is the applied stress range, A is the intercept of the curve with the y-axis in logarithmic scale, and B is the slope of the curve. The fatigue limit was computed with the Hodges-Rosenblatt [56] method, while the standard deviation in terms of stress was computed with Equation (2).

$$\sigma_{\log S} = \frac{\sigma_{\log N}}{B} \tag{2}$$

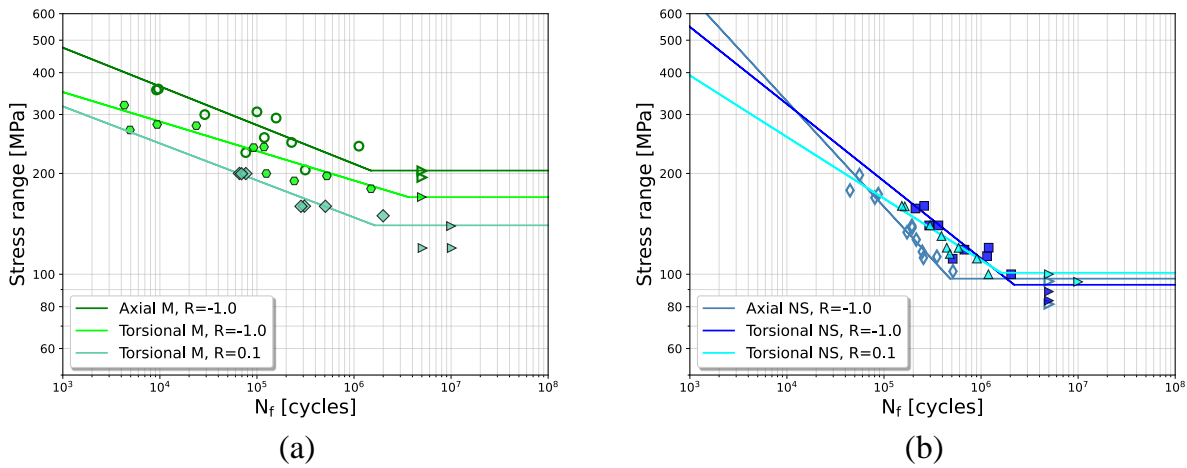The obtained fitted parameters are reported for each specimen series in Table 5.

Figure 4: Torsional fatigue tests (solid symbols) at the two torque ratios of $R_T = -1$ and $R_T = 0.1$ compared with the axial fatigue test results (hollow symbols): a) comparison between axial and torsional machined specimens and b) comparison between axial and torsional net-shape specimens. Right-pointing triangles are the *Run-Outs* tests.

The ratio between the fatigue limit in axial loading and that in torsion of the machined specimens tested in fully reversed loading ($R_L = -1$) results to be $\Delta\tau_w/\Delta\sigma_w = 0.834$, which is in line with estimation proposed by Beretta and al. [40] for cracks emanating from spherical defects subjected to torsion. A 19% reduction of the fatigue limit between the tests at $R_T = -1$ and and those at $R_T = 0.1$ was observed. In the finite life regime the slope of the S-N curves of the tensile and torsional specimens for load ratio $R_L = -1$ are comparable, while the $R_L = 0.1$ tests have a slope of the curve less steep than those of fully reversed tests.

Differently from the machined test results those net-shape specimens show a small difference between the fatigue limit in torsion and that in axial, resulting in a ratio between them equal to $\Delta\tau_w/\Delta\sigma_w = 0.96$. Furthermore, no significant difference between the fatigue limits of fully reversed tests and those at $R_L = 0.1$ is detected. The slopes of the S-N curves of the torsional tests at the two load ratios ($R_L = -1$ and $R_L = 0.1$) in the finite life are comparable, and slightly less steep than that for the axial one. Torsional tests show on average a fatigue life slightly longer than those tested under axial loading. This can be due to the stress gradient under torsional loading in which the stress is maximum on the external surface, while it decreases

in the thickness, resulting a slower crack growth as compared to the one in axial specimens.

Table 5: Fatigue limits and S-N parameters of axial and torsional tests performed on machined and net-shape specimens.

Series	Test type	Surface state	Load ratio	ΔS_{lim} [MPa]	A	B	$\sigma_{\log N}$	$\sigma_{\log S}$	N_k [cycles]
Series B	Axial	Machined	-1.0	204	26.1473	-8.6478	0.2632	0.0304	1490399
Series G	Axial	Net-shape	-1.0	97	11.9896	-3.1744	0.0844	0.0266	478478
Series D	Torsional	Machined	-1.0	170	31.8858	-11.3544	0.2920	0.0257	3634097
Series C	Torsional	Machined	0.1	140	25.6270	-9.0461	0.1803	0.0199	1632726
Series E	Torsional	Net-shape	-1.0	93	14.8843	-4.3394	0.1412	0.0325	2200883
Series F	Torsional	Net-shape	0.1	101	17.1357	-5.4493	0.1817	0.0334	1584900

3.3. Analysis of fracture surfaces

The analysis of some of the fracture surfaces of the tested specimens are reported in Figure 5 and Figure 6, for machined and net-shape specimens respectively.

All machined axial specimens failed due to defects near the specimen's external surface. Two defect families were found: a) lack of fusions (LoFs) with an irregular shape, two of which are shown in Figure 5.a and Figure 5.b and b) pores with a well defined spherical shape, two of which are shown in Figure 5.c and Figure 5.d. Torsional specimens all failed due to inclined fatigue cracks starting from a defect located close to the external surface, oriented as the maximum principal stress plane. This was observed for both fully-reversed and $R_T = 0.1$ torsional tests; typical crack paths for the two torque ratios are shown in Figure 5.e and Figure 5.g, respectively. As in the case of axial tests, all torsional specimens failed due to pores or LoFs. Cracks starting from pores nucleated and propagated onto the maximum principal stress plane. However, cracks starting from LoFs nucleated on the maximum shear plane perpendicular to the main specimen's axis. Some of the fracture surfaces are shown in Figure 5.f and Figure 5.h for fully-reversed and $R_T = 0.1$ torsional tests, respectively.

Fatigue cracks responsible to the final failure of net-shape axial specimens all started from external surfaces, that were triggered by both superficial features related to the rough surface (Figure 6.a and Figure 6.b) and spherical powder particles (SPP) (Figure 6.c and Figure 6.d). The superficial features (Figure 6.a, Figure 6.b and Figure 6.f) can be considered as elongated superficial cracks. This kind of defects, if loaded in torsion, start propagating in Mode III at the deepest point and in Mode II on the surface, then the crack shifted in Mode I along the maximum principal stress plane. An evidence of this mechanism can be observed in Figure 6.e which shows a typical crack path due to a superficial feature. The corresponding SEM analysis of the fracture surface is shown in Figure 6.f. On the other side, SPPs attached to the external surface can be considered as spherical defects, with the same crack propagation mechanism observed in cracks started from pores in the machined specimens. For these defects the crack nucleated and propagated along the maximum principal stress plane. In Figure 6.g, a crack path of one of the specimens that failed due to this mechanism is shown, while the SEM analysis of this defect is shown in Figure 6.h.
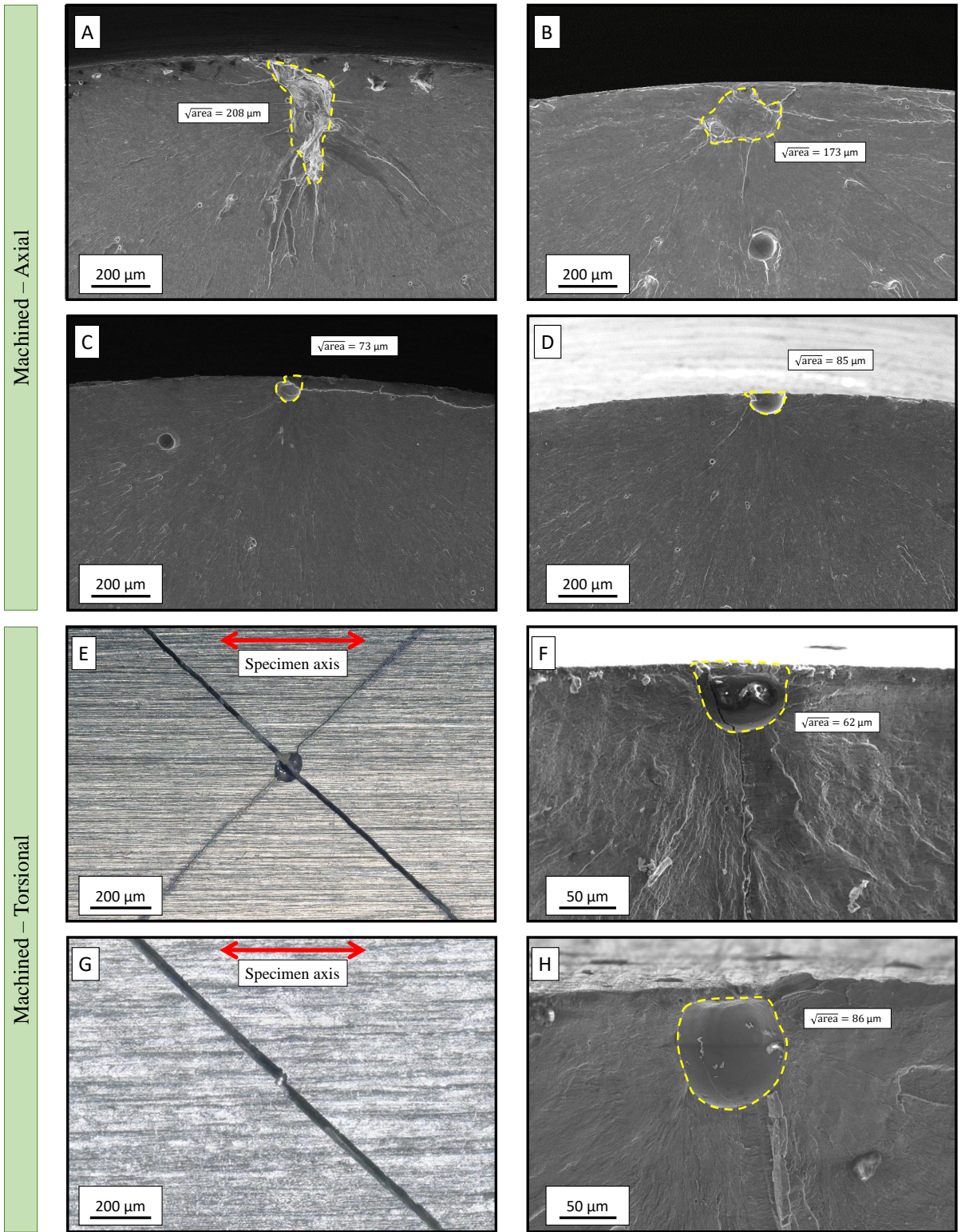
16

Figure 5: Comparison between axial and torsional crack initiating defects in machined specimens: a) LoFs defect, $\Delta\sigma = 204.81\,\text{MPa}$ $N_f = 314\,622$ cycles; b) LoFs defect, $\Delta\sigma = 299.74\,\text{MPa}$ $N_f = 29\,002$; c) pore defects $\Delta\sigma = 241.26\,\text{MPa}$ $N_f = 1\,122\,736$ cycles; d) pore defects $\Delta\sigma = 292.72\,\text{MPa}$ $N_f = 157\,527$ cycles; e)-f) torsional specimen failed by pore, $R_T = -1$ $\Delta\tau = 180\,\text{MPa}$ $N_f = 1\,497\,325$ cycles; g)-h) torsional specimen failed by pore, $R_T = 0.1$ $\Delta\tau = 120\,\text{MPa}$ $N_f = 5\,000\,000$ cycles (run-out).
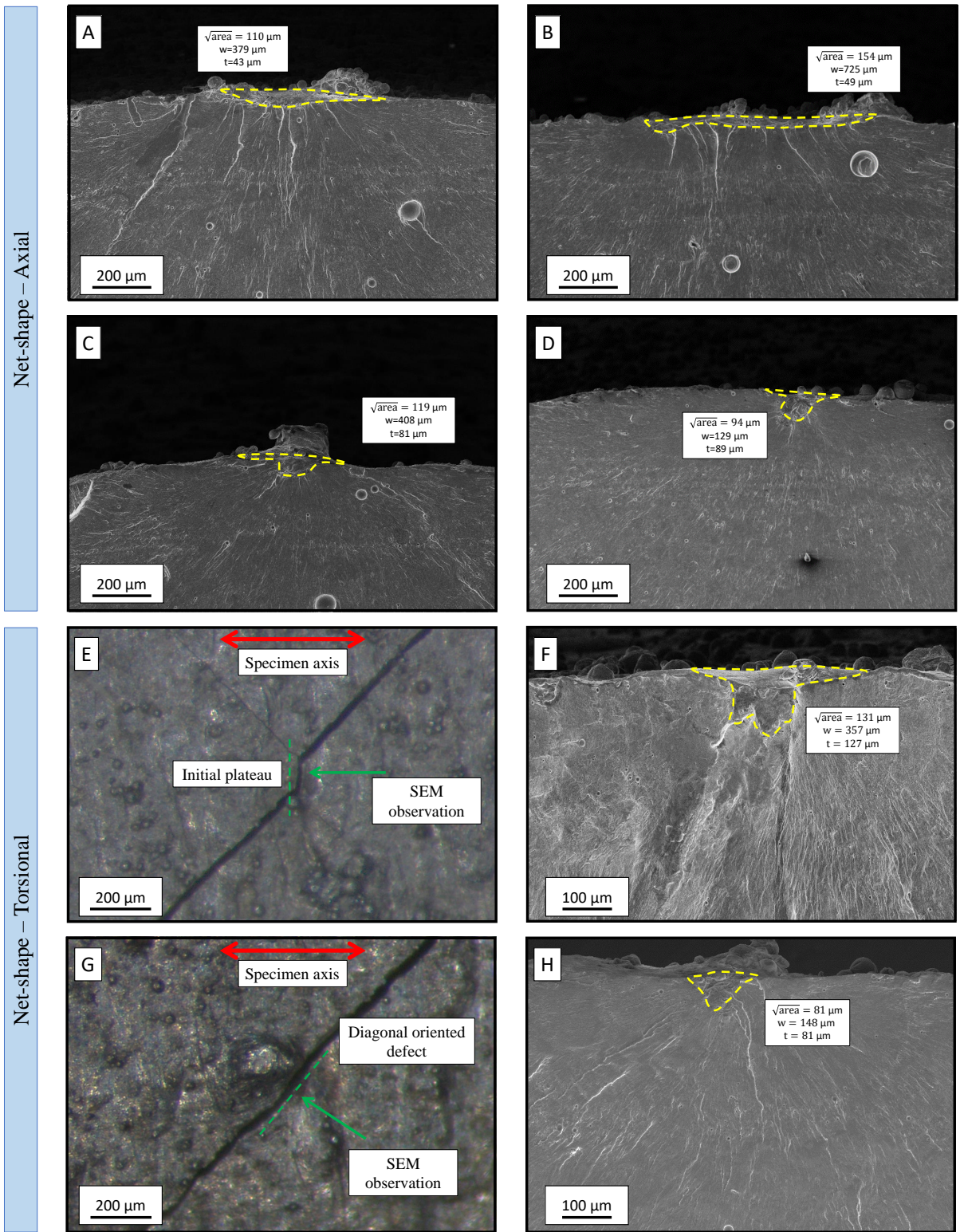
Figure 6: Comparison between axial and torsional crack initiating defects in net-shape specimens: a) superficial features, $\Delta\sigma = 197.77\,\text{MPa}$ $N_f = 55\,864$ cycles; b) superficial features, $\Delta\sigma = 111.99\,\text{MPa}$ $N_f = 254\,929$ cycles; c) SPP defects, $\Delta\sigma = 178.02\,\text{MPa}$ $N_f = 44\,670$ cycles; d) SPP defects, $\Delta\sigma = 133.44\,\text{MPa}$ $N_f = 172\,806$; e)-f) torsional specimen failed by superficial feature, $R_T = -1$ $\Delta\tau = 120\,\text{MPa}$ $N_f = 1\,198\,800$ cycles; g)-h) torsional specimen failed by SPP, $R_T = 0.1$ $\Delta\tau = 130\,\text{MPa}$ $N_f = 390\,500$ cycles.

18

3.4. Residual stress measurements

To evaluate the stress tensor due to the presence of manufacturing residual stresses, two torsional net-shape specimens were analysed with an X-ray diffractometer (XRD). Four measurements at different depths from the free specimen's surfaces were performed, namely $0\,\mu m$, $50\,\mu m$, $100\,\mu m$ and $500\,\mu m$; these measurements were repeated two times for each specimen, one for both opposite surfaces. Each measurement consists on the evaluation of the stresses directed parallel ($\Theta = 0°$), perpendicular ($\Theta = 90°$) and $45°$ ($\Theta = 45°$) with respect to the specimen's main axis. The results of the residual stresses analysis are reported in Table C.10 of the Appendix C, A and B are the two opposite specimen's surfaces, respectively.

The residual stresses of other two net-shape axial specimens were measured only along the main and tangential axes. Being the gripping zones cylindrical, three measurements were performed equally spaced of $120°$ each. The two specimens were analysed at three depths of $0\,\mu m$, $50\,\mu m$ and $100\,\mu m$; the same erosion strategy was repeated onto another specimen with two additional deeper measurements at $300\,\mu m$ and $500\,\mu m$. To make a comparison between the net-shape and machined material, the residual stresses of a machined axial specimen were measured at the same depths previously considered up to $100\,\mu m$ depth. The results of both machined and net-shape specimens are shown in Figure 7, all the results refer to the orientations schematized in Figure 7.e. The solid green lines of Figure 7.a and Figure 7.b represent the trend of the mean residual stresses of the machined material along the two components' direction as a function of the depth, while the shaded region confined by the dashed green curves represents the $95\,\%$ scatter band of the data. Residual stresses in the machined specimens are compressive due to the machining removal process, showing a mean value of $-90\,\mathrm{MPa}$ of the component along $Z\text{-}axis$ onto the free surface that steeply approaches zero at a depth of $100\,\mu m$. The same trend can be identified for the $X\text{-}axis$ component in Figure 7.b. The solid blue lines of Figure 7.a and Figure 7.b represent the trend of the mean residual stresses along the two components' directions of the net-shape material, with the shaded region to be the $95\,\%$ scatter band. Differently from the machined material, the net-shape specimens have tensile residual stresses which are due to the consecutive melting of the powder. The mean stress value remains almost constant through the axial specimen's thickness until about $500\,\mu m$ as reported in Figure 7.c and Figure 7.d, with the same values found for the torsional specimens.

One of the torsional net-shape specimen was used to evaluate the residual stress relaxation due to the torsional loading. The specimen's surface was slightly electropolished along the gauge section to remove the first $50\,\mu m$ layer of material, in order to have a smoother finishing avoiding measurement errors due to the typical high roughness of a net-shape surface. Four different measurements were performed along the gauge section of the specimen, each equispaced of $90°$. Measurements were performed both before and after testing, interrupting the test at about the estimated specimen's mid-life to avoid cracks propagation; cracks create a discontinuity inside the material, and can completely release residual stresses. The torsional specimen was subjected to a shear range of $\Delta\tau = 115\,\mathrm{MPa}$ with a torque ratio of $R_T = 0.1$, the test was interrupted after about $200\,000$ cycles. Figure 8.a shows a scheme of the measurements' position along the gauge section, the

results of the XRD measurements are shown in Figure 8.b and reported in Table C.12 of the Appendix C. The
mean values of residual stresses found along the two directions are $\sigma_{zz} = 80.18\,\text{MPa}$ and $\sigma_{xx} = 57.63\,\text{MPa}$.
During the torsional loading, the specimen is subjected to a maximum shear stress of $\tau_{xz} = 127.78\,\text{MPa}$.
Computing the resulting *Von-Mises* stress in biaxial plane stress condition, Equation (3), it ends up:

$$\sigma_{VM} = \sqrt{\sigma_{xx}^2 - \sigma_{xx} \cdot \sigma_{zz} + \sigma_{zz}^2 + 3 \cdot \tau_{xz}^2} = 232.62\,\text{MPa} \tag{3}$$

The obtained stress is slightly above the yield limit of the material, which is $\sigma_Y = 212.2\,\text{MPa}$ as reported in
Table 3. This means that the material experienced an elastic shake-down during the loading, explaining why
the residual stresses at the end of the test are completely relaxed as shown in Figure 8.b.
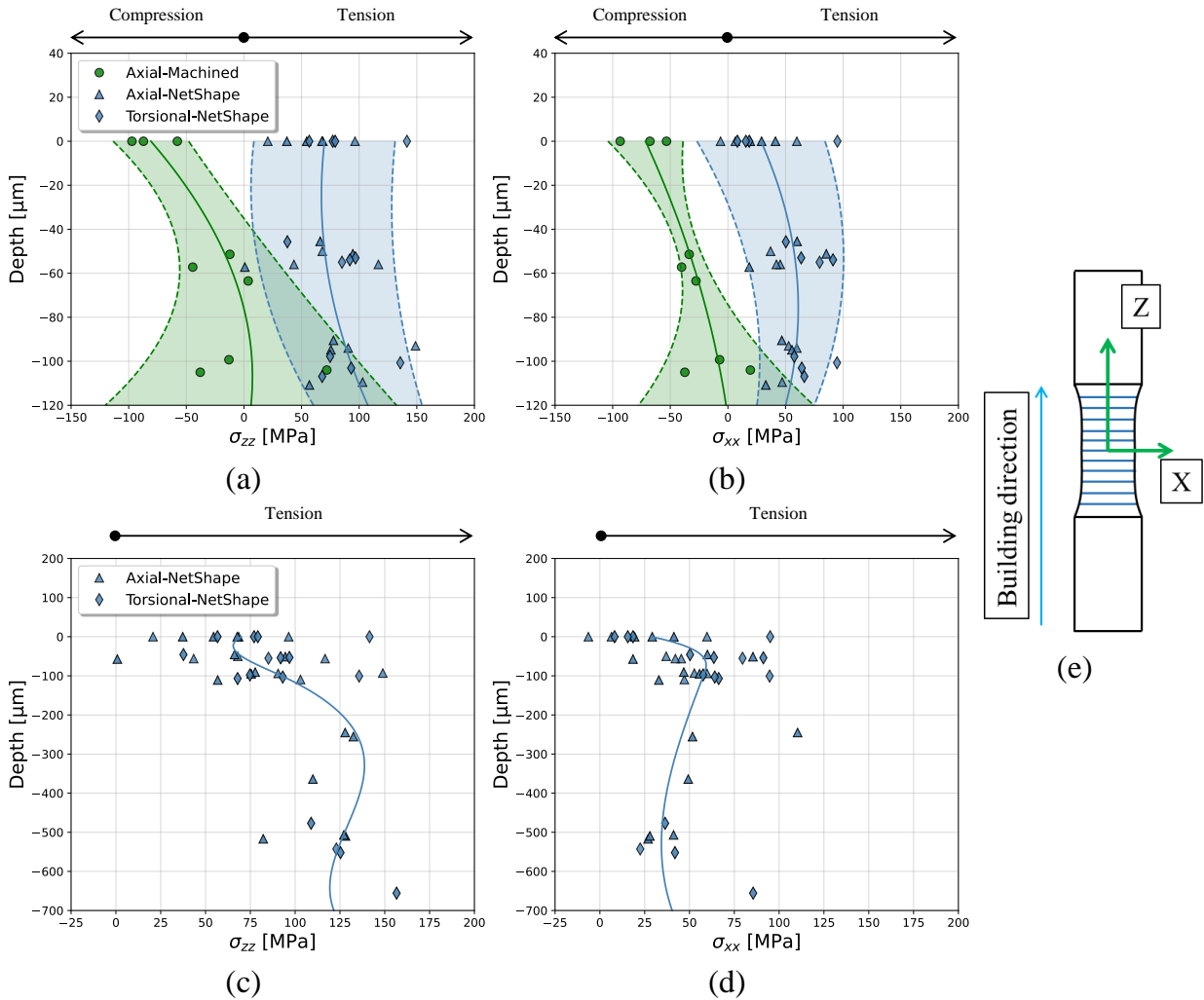

Figure 7: Comparison between residual stresses of machined and net-shape specimens: a) residual stresses along the building direction; b) residual stresses along the axis perpendicular to the building direction; c) detail of the residual stresses along the building direction for net-shape specimens; d) detail of the residual stresses along the axis perpendicular to the building direction for net-shape specimens and e) scheme of the orientation of the residual measured stress respect to the specimen's axes.
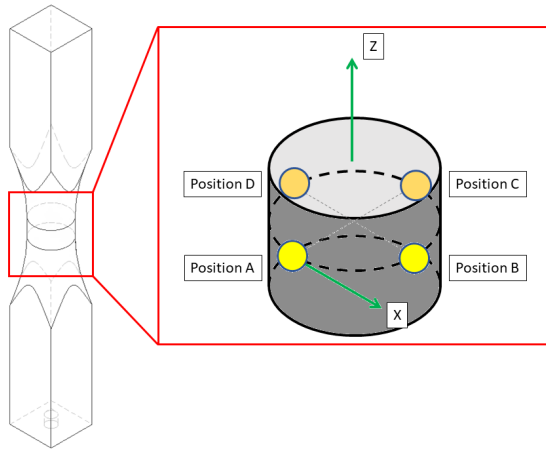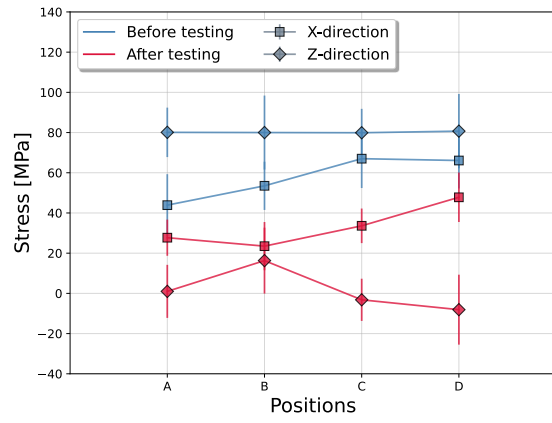
(a)   (b)

Figure 8: Analysis of residual stresses in a torsional specimen measured before testing and after a mid-life cycling: a) scheme of the measured positions on the specimen's gauge length and b) X-ray measurements results.

4. Discussion

4.1. Defect distribution and statistic of extremes

The main part of the scatter observed in fatigue results of AMed materials is due to the statistical distribution of the manufacturing defects, as shown for those internal [5, 11] and superficial [24, 25, 39] anomalies. Defects responsible to the final failure of the specimens were measured in this study according to the $\sqrt{\text{area}}$ model proposed by Murakami [8]. Superficial defects are elongated along the external specimen's surface, hence computing the $\sqrt{\text{area}}$ only based on the measured area could result in an overestimation of the SIF. To avoid this, the $\sqrt{\text{area}}$ of elongated superficial defects was computed with the following empirical rule:

- for defects with an aspect ratio $w/t < 10$, where w is the superficial length of the defect and t the depth, $\sqrt{\text{area}}$ was computed simply from the area calculated from the fracture surfaces observation;

- when the aspect ratio is $w/t \geq 10$ the $\sqrt{\text{area}}$ is calculated as:

$$\sqrt{\text{area}} = t_{\max} \cdot \sqrt{10} \tag{4}$$

where $t_{\max}$ is the maximum depth of the defect. This rule was shown to work well in case of elongated 2D cracks and surface roughness [8, 24, 25, 57]. The dimension of the found defects for each specimen are reported in Table A.8 and Table B.9 in Appendix A and Appendix B for machined and net-shape specimens respectively.

These defects represent the critical defects in terms of fatigue strength and hence the prospectively maxima for the machined and net-shape specimens. They can be then analysed, according to the theory of statistics of extremes, with a *Largest Extreme Value Distribution* (LEVD), which the cumulative density function is reported in Equation (5):

$$F_{\text{LEVD}} = \exp\left[-\exp\left(-\frac{x-\lambda}{\delta}\right)\right] \tag{5}$$

where x is the defect size, λ is the location and δ the scale parameter. The parameters λ and δ where computed with the *momentum equations* [58], and are reported in Table 6. The obtained probability plots are shown in Figure 9.a and Figure 9.b for machined and net-shape specimens, respectively, where the solid lines represent the regression line obtained by fitting the experimental data while the shaded areas confined by the dashed lines are the bilateral 95 % confidence bands.

As extensively discussed in Subsection 3.3, in machined specimens two families of defects were found, namely pores and LoFs. This two families can be perfectly distinguished on the probability plot of Figure 9.a; both pores and LoFs found for the two loading conditions perfectly match one to another. The scale parameter δ, which can be geometrically interpreted as the slope of the regression line on the probability plot, is higher for axial specimens as compared to the torsional ones. A major portion of the torsional specimens failed due

22

to pores, which are usually smaller than LoFs leading to a regression line on the LEVD steeper than that of the axial tests.

The obtained distributions for the net-shape specimens tested in the two loading conditions are very similar; this can be also noted by analysing the values of the scale parameter δ that are comparable. The location parameter λ is instead different, with a smaller value for the torsional specimens leading to a defect distribution shifted on the left with respect to that of the axial loading. This evidence indicates that the defects responsible to the final failure of the torsional specimens are a bit smaller that those loaded axially. The difference in the size of defects between the two loading conditions can be explained considering the direction of the principal stress:

- in case of axial loading the principal stress is oriented as the main specimen's axis, which is perpendicular to the printing plane. On this plane the effective $\sqrt{\text{area}}$ of the superficial features is maximum;

- for torsional loading the propagation plane (i.e., principal stress direction) tends to be oriented $45°$ with respect to the main specimen's axis. The projection of the $\sqrt{\text{area}}$ on this plane is hence smaller than the case of axial loading condition.

Table 6: Fitted parameters of the LEVD for machined and net-shape specimens.

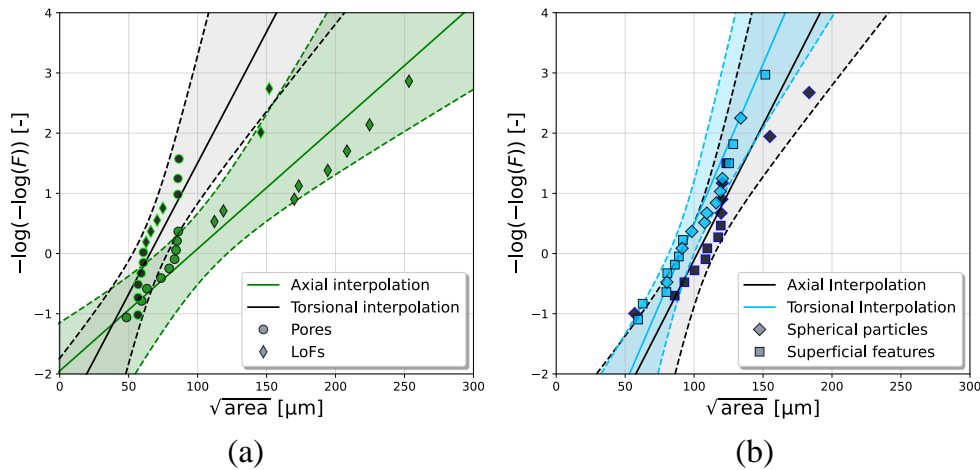| Test type	Surface state	λ [mm]	δ [mm]
Axial	Machined	0.0961	0.0493
Torsional	Machined	0.0654	0.0229
Axial	Net-shape	0.1023	0.0223
Torsional	Net-shape	0.0908	0.0188

Figure 9: Comparison between axial and torsional LEVD of killer defects: a) machined specimens and b) net-shape specimens.

4.2. Mechanisms of crack propagation and fatigue limit

As reported in the analysis of fracture surfaces, the specimens tested under torsional loading showed two different failure mechanisms. The first of which is associated with a fatigue crack emanating from a spherical defect, which nucleates and propagates along the maximum principal stress plane until failure. The second failure mechanism is triggered from superficial features or irregularly elongated LoFs. These defects can be considered as elongated cracks, that start propagating under torsional loads in Mode II on the surfaces then branching in Mode I along the maximum principal stress plane until failure. A schematic representation of these two mechanisms is shown in Figure 10 and Figure 11, respectively.

$\sigma_3 = -\tau$ $\sigma_1 = \tau$

$\sigma_1 = \tau$ $\sigma_3 = -\tau$

τ

τ

(a)

Machined

Specimen axis

200 μm

$\sqrt{area} = 67$ μm

Spherical pore

50 μm

(b)

Net-shape

Specimen axis

200 μm

Spherical particles

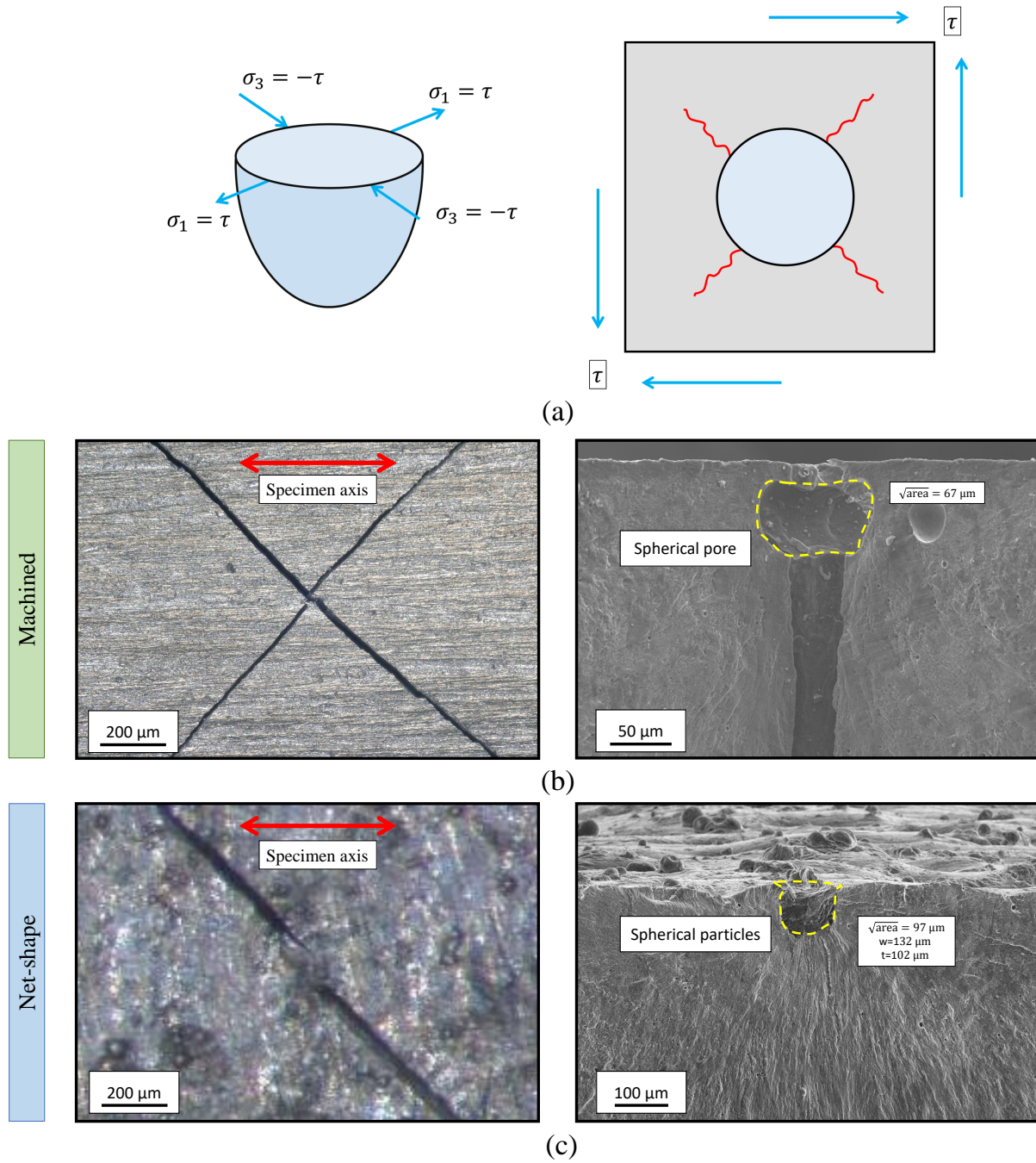$\sqrt{area} = 97$ μm
w=132 μm
t=102 μm

100 μm

(c)

Figure 10: Failure mechanisms of fatigue cracks under torsional loading in case of spherical defects: a) schematic of the mechanism; b) example of a machined specimen failed due to a spherical pore and c) example of a net-shape specimen failed due to a SPP.
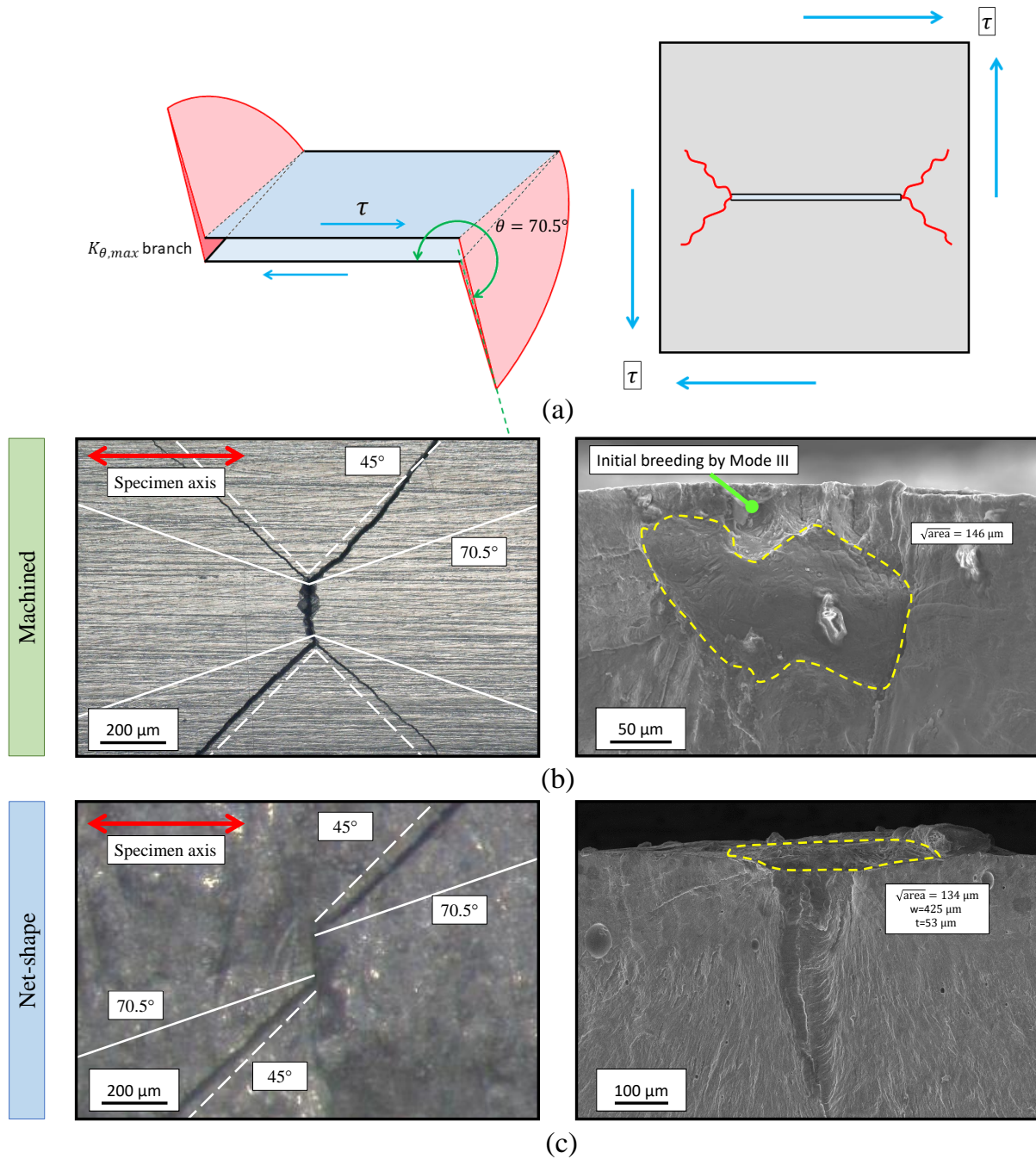
Figure 11: Failure mechanisms of fatigue cracks under torsional loading in case of elongated defects: a) schematic of the mechanism; b) example of a machined specimen failed due to an elongated LoF and c) example of a net-shape specimen failed due to a superficial feature.

For both the mechanisms found, the final failure happens onto the maximum principal stress plane, with the cracks inclined 45° with respect to the specimen's main axis. We then speculate on this observation that the non propagating condition for a crack emanating from a defect corresponds to the crack fatigue threshold in Mode I. This hypothesis is also confirmed from fatigue tests in torsion performed on different

materials [43, 44, 45, 59]. The objective of this chapter is thus to find an appropriate formulation for the evaluation of SIF for torsional cracks emanating from manufacturing defects that branched in Mode I inclined cracks.

Considering the loading condition in terms of principal stresses acting on a spherical defect loaded in torsion, shown in Figure 10.a, it can be seen that it is loaded in tension along the first principal stress direction and in compression along that third. If the defect is considered as a small notch, the biaxial state of stress due to the torsional load produces a stress concentration factor of $K_t = 4$, which is higher than the pure axial loading condition $K_t = 3$ [8]. The stress concentration factor is directly related to the SIF, meaning that torsional loading is more deleterious than that of pure axial in case of spherical defects or cavities. Beretta et al. [40] analysed the SIFs for cracks emanating from different defect geometries under shear loadings using the formulation proposed by Shiratori et al. [60]. With these analyses, they demonstrated that the ratio between the fatigue range limit in torsion and that in axial/bending is equal to the ratio between the SIF in Mode I due to tension and that in shear. In particular this ratio is a constant and can be approximated as Equation (6):

$$\frac{\Delta\tau_{\text{w}}}{\Delta\sigma_{\text{w}}} = \frac{\Delta K_{\text{I,tens}}}{\Delta K_{\text{I,shear}}} = 0.855 \pm 0.025 \tag{6}$$

where $\Delta K_{\text{I,tens}}$ is the SIF range for Mode I cracks under tension load, and $\Delta K_{\text{I,shear}}$ is the SIF range form Mode I cracks under shear load.

Considering this relation, the SIF range in shear of the found spherical defects can be thus computed, starting from that for uniaxially loaded specimens containing irregular surface defects [61, 62], Equation (7):

$$\Delta K_{\text{I,tens}} = 0.65 \cdot \Delta\sigma_1 \cdot \sqrt{\pi \cdot \sqrt{\text{area}}} \tag{7}$$

where $\Delta\sigma_1$ is the maximum principal stress range and $\sqrt{\text{area}}$ the square root of the defect's area. The SIF range for Mode I cracks loaded in shear can thus be obtained from Equation (8):

$$\Delta K_{\text{I,shear}} = \frac{\Delta K_{\text{I,tens}}}{0.855} \tag{8}$$

This mechanism was found to happen in both machined and net-shape specimens. As shown in Figure 10.b machined specimens failed due to cracks triggered by spherical pores. During the laser scanning process, some fused particles can be ejected from the moving melt pool, which become solidified and land on the powder bed, sometimes they impact the specimen's surface and create SPP. These features are responsible to trigger this mechanism on the net-shape as shown in Figure 10.c.

It was observed that part of the tested specimens failed from cracks that nucleated in Mode II along the surface, then branched in Mode I along the maximum principal stress planes as schematically reported in Figure 11.a. This mechanism is the same as the one analysed by Murakami et al. in [43] for an initially pre-cracked medium carbon steel. Elongated defects, LoFs or superficial features, can be considered as

horizontal semi-elliptical cracks parallel to the building plane. Given a semi-elliptical crack loaded in torsion, the direction of crack propagation along the maximum tensile plane can be computed with the $\sigma_{\theta,\max}$ model proposed by Erdogan and Sih [63]. The tensile, σ_θ, and the shear stress, $\tau_{r,\theta}$, in the vicinity of the crack tip can be expressed as Equation (9):

$$
\begin{aligned}
\sigma_\theta &= \frac{1}{\sqrt{2 \cdot \pi \cdot r}} \cos\left(\frac{\theta}{2}\right) \left[K_I \cdot \cos\left(\frac{\theta}{2}\right)^2 - \frac{3}{2} \cdot K_{II} \cdot \sin\left(\theta\right) \right] \\
\tau_{r,\theta} &= \frac{1}{2 \cdot \sqrt{2 \cdot \pi \cdot r}} \cos\left(\frac{\theta}{2}\right) \left[K_I \cdot \sin\left(\theta\right) + K_{II} \cdot \left(3 \cdot \cos\left(\theta\right) - 1\right) \right]
\end{aligned}
\tag{9}
$$

420   The direction that maximizes σ_θ is given by equating the shear stress $\tau_{r,\theta}$ to zero, Equation (10):

$$
K_I \cdot \sin\left(\theta_0\right) + K_{II} \cdot \left(3 \cdot \cos\left(\theta_0\right) - 1\right) = 0
\tag{10}
$$

The direction for pure Mode II is hence along $\theta_0 = \pm 70.5°$. Given the stress intensity factor considering σ_θ is thus defined as, Equation (11):

$$
K_{\theta,\max} = \sigma_\theta \cdot \sqrt{2 \cdot \pi r} = \cos\left(\frac{\theta_0}{2}\right) \cdot \left[K_I \cdot \cos\left(\frac{\theta_0}{2}\right)^2 - \frac{3}{2} \cdot K_{II} \cdot \sin\left(\theta_0\right) \right]
\tag{11}
$$

Substituting $\theta_0 = \pm 70.5°$ in Equation (11), the maximum value of K_θ for pure Mode II becomes Equation (12):

$$
K_{\theta,\max} = 1.155 \cdot K_{II}
\tag{12}
$$

425   The value of SIF for semi-elliptical cracks in Mode II can be computed through the equations proposed by Sih and Kassir [64] for different crack's aspect ratios a/c, where a is the crack depth and c is the half superficial length. A direct relation between the SIF and the shear stress, like Equation (7), cannot be hence applied for torsional loads due to the different crack shape factors for each aspect ratio. Hence Murakami et al. [43] proposed the adoption of Equation (13):

$$
\Delta K_{\theta,\max} = F \cdot \Delta\tau \cdot \sqrt{\pi \cdot \sqrt{\text{area}}_{\text{p}}}
\tag{13}
$$

430   where $\sqrt{\text{area}}_{\text{p}}$ is the projected square root area along the maximum principal stress plane ($\sqrt{\text{area}}_{\text{p}} = \sqrt{\text{area}} \cdot \cos\left(45°\right)$) and F is the shape factor of Mode II semi-elliptical cracks given by Equation (14):

$$
F = 0.0957 + 2.11 \cdot (a/c) - 2.26 \cdot (a/c)^2 + 1.09 \cdot (a/c)^3 - 0.196 \cdot (a/c)^4
\tag{14}
$$

This model was found to well describe the failure mechanisms of both machined and net-shape specimens. Initial Mode II cracks were found to start from LoFs, which are elongated on the printing plane [65]. As shown in Figure 11.b, the very first propagation of the crack was onto the plane oriented at about 70.5°,

28

and then the crack continued to propagate onto the maximum principal stress plane until the final failure along the maximum tensile plane oriented at 45° with respect to the main specimen's axis. As shown in Figure 11.b traces of the initial Mode III propagation of the LoF toward the surface can be also noted. For the net-shape specimens this mechanism was triggered by superficial features due to the irregular rough surface, Figure 11.c. For this kind of defects, the first propagation stage is also onto the 70.5° oriented plane, with the final failure happening on that maximum tensile.

Supposing to be in LEFM conditions, the axial fatigue limit $\Delta\sigma_\mathrm{w}$ can be computed from the long crack threshold by inverting Equation (7) for a certain defect dimension; the torsional fatigue limit $\Delta\tau_\mathrm{w}$ can be as well computed by inverting Equation (13). Considering the mean value of the found LoFs and superficial defects, the axial and torsional fatigue mean strengths can be then computed; for torsional loading, a mean aspect a/c ratio is computed from experimental observations, which results in 0.4177 and 0.4791 for machined and net-shape specimens, respectively. The ratios $\Delta\tau_\mathrm{w}/\Delta\sigma_\mathrm{w}$ for machined and net-shape specimens can be then computed, the results are shown in Table 7. The found values are in agreement with the experimental results shown in Section 3.2.

Table 7: Ratios between torsional and axial fatigue limits for LoFs (machined specimens) and superficial features (net-shape specimens).

	LoF	Superficial features
$\Delta\tau_\mathrm{w}/\Delta\sigma_\mathrm{w}$	0.9905	0.9321

5. Fatigue threshold model under axial and torsional loads

5.1. Uniaxial fatigue strength

The fatigue strength of AMed materials can be linked to the manufacturing defects size through the adoption of Kitagawa-Takahashi diagram, which can also take into account the effect of short cracks considering the El-Haddad model [66]. The fatigue limit can be thus computed as a function of $\sqrt{\mathrm{area}}$ parameter from Equation (15):

$$\Delta\sigma_\mathrm{w} = \Delta\sigma_\mathrm{w0} \cdot \sqrt{\frac{\sqrt{\mathrm{area}}_0}{\sqrt{\mathrm{area}}_0 + \sqrt{\mathrm{area}}}} \tag{15}$$

where $\Delta\sigma_\mathrm{w0}$ is the fatigue limit of the defect-free material and $\sqrt{\mathrm{area}}_0$ is the El-Haddad parameter. This is defined as, Equation (16):

$$\sqrt{\mathrm{area}}_0 = \frac{1}{\pi} \cdot \left(\frac{\Delta K_\mathrm{th,lc}}{Y \cdot \Delta\sigma_\mathrm{w0}} \right)^2 \tag{16}$$

where $Y = 0.65$ is the Murakami's boundary correction factor for surface defects and $\Delta K_\mathrm{th,lc}$ is the long crack propagation threshold.

As shown in Section 3.4, both machined and net-shape specimens are affected by the presence of residual stresses. Residual stresses can be considered as a mean stresses applied to the specimen, leading to an effective stress ratio during the fatigue cycling. Irrespectively of the sign of the residual stresses, the maximum and

minimum value of the effective stresses applied to the specimen during the fatigue cycling can be computed from Equation (17):

$$\sigma_{\text{max}}^{\text{eff}} = \frac{\Delta\sigma}{(1 - R_L)} + \sigma_{\text{RS}}$$

$$\sigma_{\text{min}}^{\text{eff}} = \frac{\Delta\sigma}{(1 - R_L)} \cdot R_L + \sigma_{\text{RS}}$$

(17)

Thus, the effective stress ratio can be computed from Equation (18):

$$R_{\text{eff}} = \frac{\sigma_{\text{min}}^{\text{eff}}}{\sigma_{\text{max}}^{\text{eff}}}$$

(18)

465   It needs to be highlighted that both the defect-free fatigue limit, $\Delta\sigma_{\text{w0}}$, and the long crack propagation threshold, $\Delta K_{\text{th,lc}}$, are functions of the effective stress ratio. The defect-free fatigue limit, $\Delta\sigma_{\text{w0}}$, can be estimated at different stress ratios with the adoption of an *Haigh* diagram, that, given the fatigue limit for the fully reversed loading and the ultimate tensile stress (UTS), can be approximated with the *Goodman* model as reported in Equation (19):

$$\Delta\sigma_{\text{w0}} = \frac{1}{\frac{1}{\Delta\sigma_{\text{w0,R=-1}}} + \frac{1}{\text{UTS}} \cdot \frac{1+R_{\text{eff}}}{1-R_{\text{eff}}}} \quad R_{\text{eff}} \geq -1$$

$$\Delta\sigma_{\text{w0}} = \Delta\sigma_{\text{w0,R=-1}} \qquad\qquad R_{\text{eff}} < -1$$

(19)

470   where $\Delta\sigma_{\text{w0,R=-1}}$ is the fatigue limit for the defect-free material in fully reversed axial loading. This quantity is generally approximated as the stress that corresponds to a plastic strain of 0.05 % of the stabilized curve [67]. Using this method with the cyclic parameters reported in Table 4, the value of the defect-free material for the fully reversed loading results $\Delta\sigma_{\text{w0,R=-1}} = 315.8$ MPa. If the cyclic properties of the material are not available, the defect free material can be approximated considering the standard tensile properties [68, 69] as

475   $\Delta\sigma_{\text{w0,R=-1}} = 2 \cdot (0.4 \cdot \text{UTS})$. By adopting the tensile parameters reported in Table 3, it results $\Delta\sigma_{\text{w0,R=-1}} = 305.2$ MPa which is close to the value estimated with the cyclic curve. The long crack propagation threshold, $\Delta K_{\text{th,lc}}$, can be instead estimated with the NASGRO curve for different stress ratios. Further details about the models and the parameters of AMed AlSi10Mg material can be found in the recent work by Beretta et al. [68].

480   The computed Kitagawa curves are compared with the experimental results in Figure 12.a and Figure 12.b for machined and net-shape specimens, respectively. The solid lines represent the effective curves taking into account the effect of residual stresses, while those dashed lines are computed considering the applied load ratio ($R_L = -1$ for the both surface states). As can be noted both specimen types are well described with the effective curves, which reflect a slight increment for the fatigue performance in presence of compressive residual

485   stresses (machined specimens, Figure 12.a) and a deleterious effect in case of tensile residual stresses (net-shape specimens, Figure 12.b). Especially for the case of net-shape specimens, a Kitagawa curve estimated by

neglecting the effect of residual stresses can lead to an overestimation of the fatigue limit given the dimension of the superficial defects.
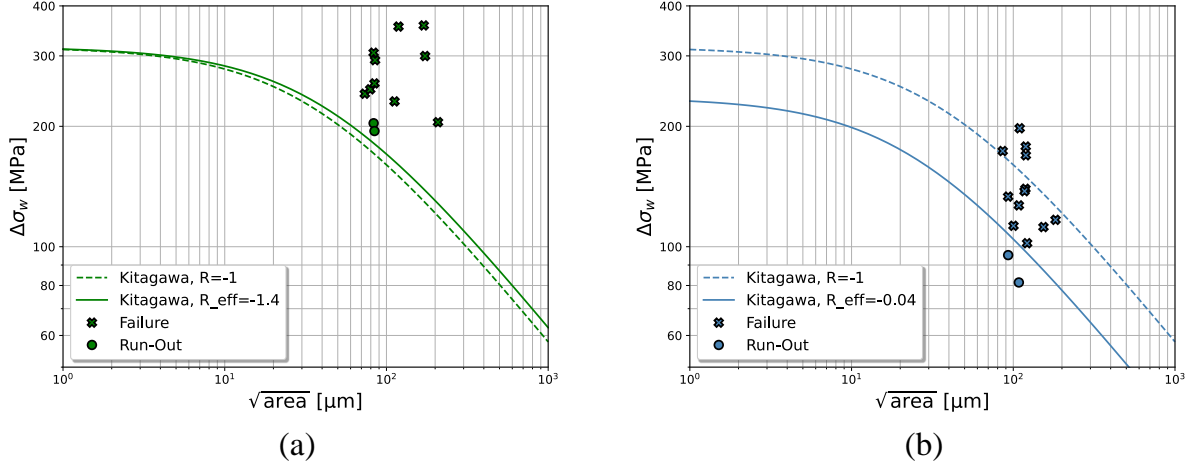

Figure 12: Kitagawa diagrams for axial loading compared with the experimental results: a) machined specimens and b) net-shape specimens.

5.2. Torsional fatigue strength

490   The aim of this *Section* is to find a relationship between the torsional fatigue limit and the dimension of the crack initiating defects. As discussed in Section 4.2, the non propagation condition for cracks subjected to torsional loads coincides with the threshold in Mode I for branching cracks along the maximum principal stress plane. Considering this evidence, a link between the defect dimension and the fatigue threshold can be estimated through the Kitagawa-Takahashi diagram considering the El-Haddad modification, Equation (20):

$$\Delta K_{\text{th}} = \Delta K_{\text{th,lc}} \cdot \sqrt{\frac{\sqrt{\text{area}}}{\sqrt{\text{area}}_0 + \sqrt{\text{area}}}} \tag{20}$$

495   As shown in Section 5.1, residual stresses play an important role in influencing the fatigue strength of the material subjected to axial loads. Being the cracks in torsion always oriented perpendicular to the maximum stress plane, the effective stress ratio has to be computed on this plane too. This can be done by considering the maximum principal stresses during the loading cycle, and rotating the residual stress tensor along this plane. The relations in Equation (17) are then modified as, Equation (21):

$$\sigma_{\text{max},1}^{\text{eff}} = \frac{\Delta\sigma_1}{(1 - R_L)} + \sigma_{\text{RS},1}$$

$$\sigma_{\text{min},1}^{\text{eff}} = \frac{\Delta\sigma_1}{(1 - R_L)} \cdot R_L + \sigma_{\text{RS},1} \tag{21}$$

31

The effective stress ratio can then be computed from Equation (22):

$$R_{\text{eff,tosion}} = \frac{\sigma_{\text{min},1}^{\text{eff}}}{\sigma_{\text{max},1}^{\text{eff}}} \tag{22}$$

As for axial tests, the $\Delta K_{\text{th,lc}}$ was computed with the NASGRO equation for different stress ratios. For each tested specimen, the corresponding SIF was computed considering the defect responsible for the final rupture and the mechanism associated with it, see Section 4.2.

The experimental results of machined specimens are compared with the obtained Kitagawa curves in Figure 13.a and Figure 13.b, for fully reversed and $R_T = 0.1$ tests, respectively. The solid lines are relative to the effective curves computed considering the effect of residual stresses, while those dashed lines are obtained considering the effective load ratios. Similar to the axial specimens, the effective curves matches reasonably well with the experimental results obtained under torsion.
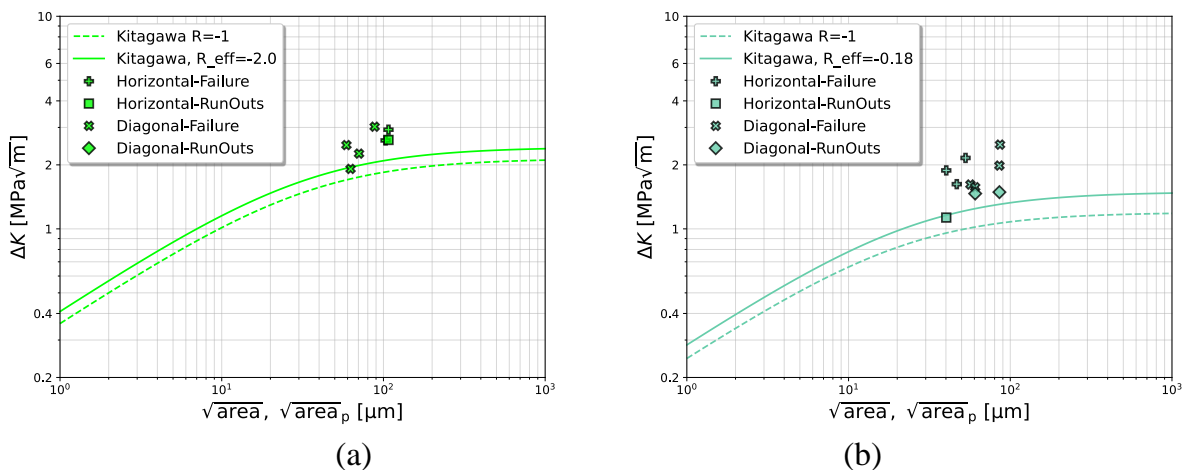

Figure 13: Kitagawa diagrams for torsional loading compared with the machined experimental results: a) tests performed at a torque ratio of $R_T = -1$ and b) tests performed at a torque ratio of $R_T = 0.1$.

The net-shape experimental results under torsion are compared with the Kitagawa curves in Figure 14.a and Figure 14.b, for fully reversed and $R_T = 0.1$ tests, respectively. The solid lines are relative to the effective curves computed considering the effect of residual stresses, while the dashed lines are obtained considering the effective load ratios. The effective curve obtained for the fully reversed torsional tests fits well with the experimental tests, similar to the previously shown results. This is apparently not true for the $R_T = 0.1$ torsional tests shown in Figure 14.b, where the experimental results lie perfectly on the effective load ratio curve. In Section 3.4, it was shown that the residual stresses are completely released at the mid-life of a torsional specimen tested at the torque ratio $R_T = 0.1$ near the fatigue limit. This means that the material is effectively cycling at the applied torque ratio, and no longer affected by the residual tensile stresses.
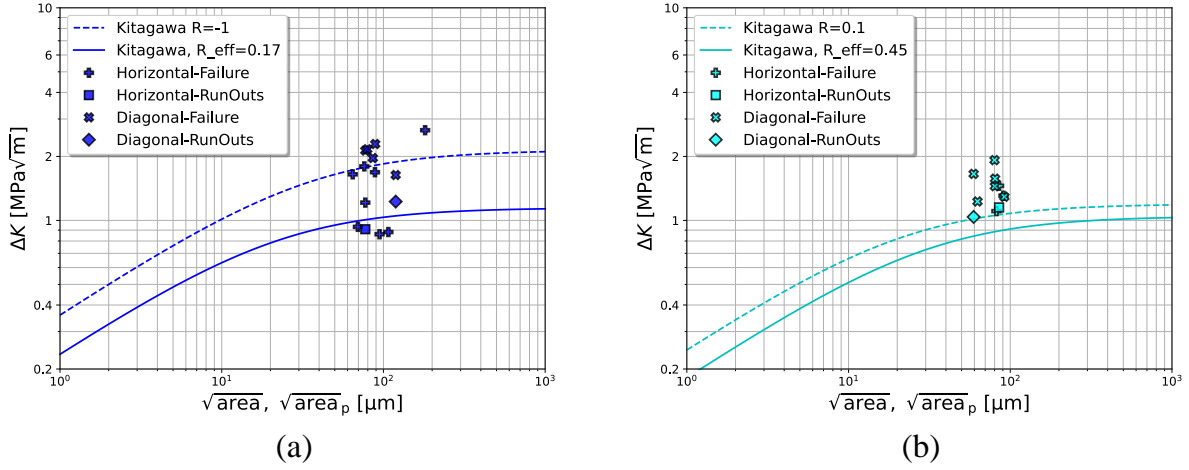
Figure 14: Kitagawa diagrams for torsional loading compared with net-shape experimental results: a) tests performed at a torque ratio of $R_T = -1$ and b) tests performed at a torque ratio of $R_T = 0.1$.

5.3. Final remarks

It has been explained in the previous chapters how to link the defect size of the tested specimens with the fatigue limit of the material taking into account the effect of residual stresses. It was shown that in case of axial loads the dimension of the killer defects between machined and net-shape materials are comparable. This means that for the analysed AlSi10Mg alloy the reduction of fatigue life between the two superficial conditions is only due to the presence of residual stresses. Machined specimens are featured by a compressive residual stress in the first layer, which can increase the fatigue performances by reducing the effective stress ratio. On the other hand, net-shape specimens are affected by tensile residual stresses that stay almost constant in the first $500\,\mu m$ depth (Figure 7.c and Figure 7.d), which reduce the fatigue performances of the specimens by increasing the effective stress ratio.

Mainly two failure mechanisms were found in torsional specimens, which were triggered by different defect geometries. The SIFs of each killer defect were then computed taking into account the failure mechanism and the $\sqrt{area}$ parameter. Cracks initiating from spherical defects where analysed with the model proposed by Beretta at al. [40], while the branching Mode I cracks from Mode II were analysed with the model proposed by Murakami et al. [43].

The two different defect families found in machined and net-shape specimens are also responsible to the different ratios between the torsion and axial fatigue limits reported in Section 3.2. For the case of spherical defects, i.e. pores and SPP, the ratio of $\Delta\tau_w/\Delta\sigma_w$ is equal to 0.855; for elongated defects the crack shape factor, F, depends on the aspect ratio. By drawing the Kitagawa diagram in stress field for uniaxial loaded specimens against that in torsion for the two mechanisms (for the elongated defects, a mean value of the aspect ratio was used) and comparing with the defect distributions of the found families it can be clearly seen that the ratio $\Delta\tau_w/\Delta\sigma_w$ for spherical defects is near 0.855, while for those elongated defects $\Delta\tau_w/\Delta\sigma_w \approx 1$. In Figure 15.a-b the LEVD distribution of the defect families for the two types of specimens are fitted. From

the found parameters the 95 % scatter bands are compared with the Kitagawa curves in Figure 15.c-d, where the shaded regions represent the defect distributions. The Kitagawa curves in torsion are computed from the expression of SIF, so they cannot capture the effect of small defects as those for uniaxial loads. Thus, they can be considered reliable up to almost 100 µm, below which the curve can start to approach the fatigue limit
545 in torsion for the defect-free specimens, that were not available.

Considering the expected results, schematically reported in Figure 1.a, it was shown that the difference of the Kitagawa curves in axial/bending and in torsion depends on the type of defect responsible of the final failure of the specimen. Spherical defects can decrease the fatigue limit in torsion by about 14.5 % with respect to that axial, representing the lower limit leading to the main part of failures due to pores observed
550 for machined specimens; this is not valid for elongated defects that, considering the mean aspect ratio of the tested material, almost coincides with the fatigue limit in axial/bending. From the point of view of fatigue limit at different torque ratios, it was expected a decreasing for both the specimens' series due to the mean load effect shown in Figure 1.b. From the experimental results, a reduction of fatigue strength with the increasing mean load was observed for the machined specimens as shown in Figure 16. For the
555 net-shape specimens the residual tensile stresses negatively affected the fatigue performances by increasing the effective stress ratio. In the case of $R_T = 0.1$, instead, the residual stresses were relaxed due to the yielding of material. These two factors make the fatigue limit at the two torque ratios comparable, contrarily to the expected trend shown in Figure 1.b.

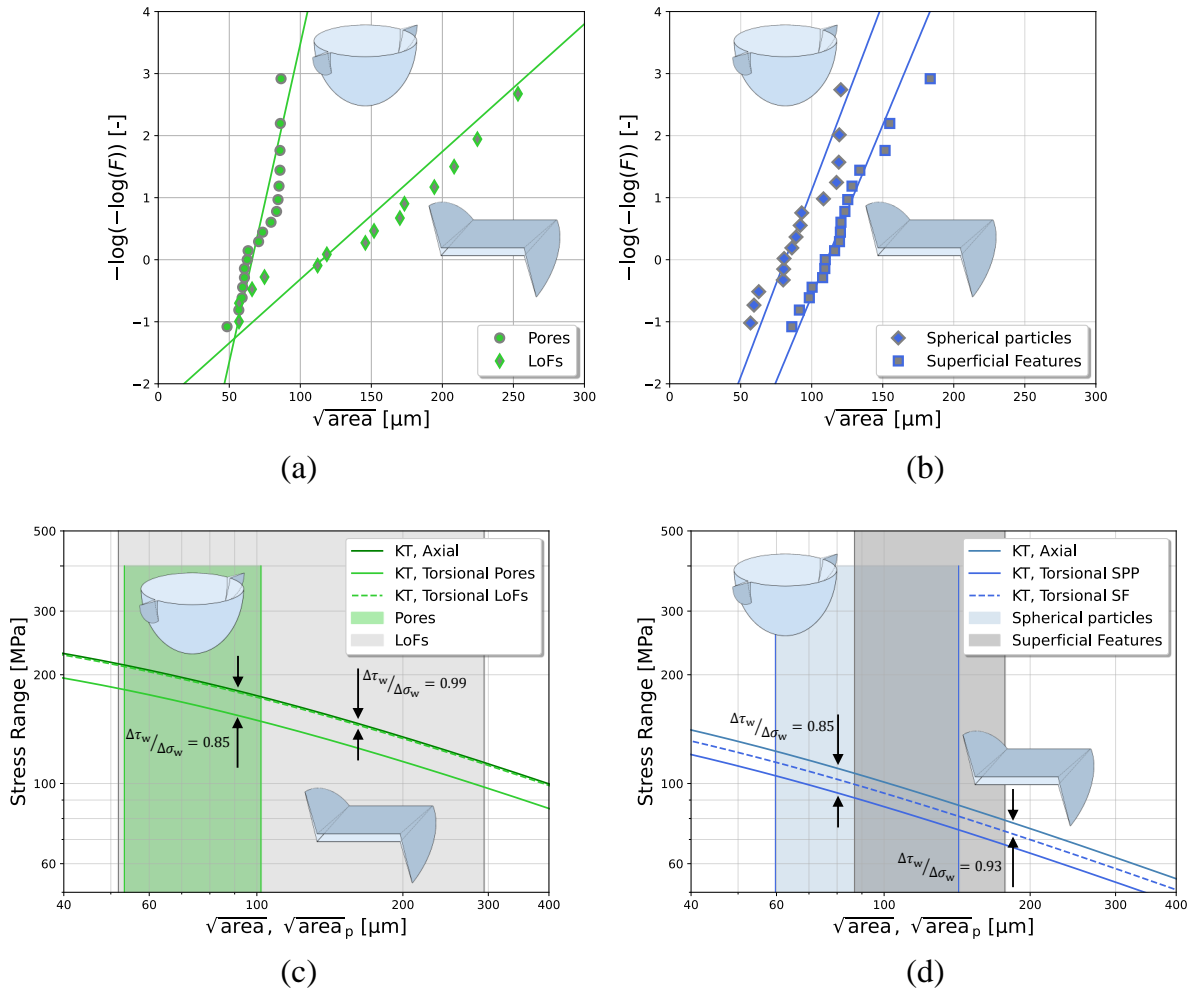**Figure 15:** Summary of the results obtained: a) LEVD of the pores and LoFs found in machined specimens; b) LEVD of the SPP and the superficial features found in net-shape specimens; c) Kitagawa diagram in stress field for machined specimens and d) Kitagawa diagram in stress field for net-shape specimens.
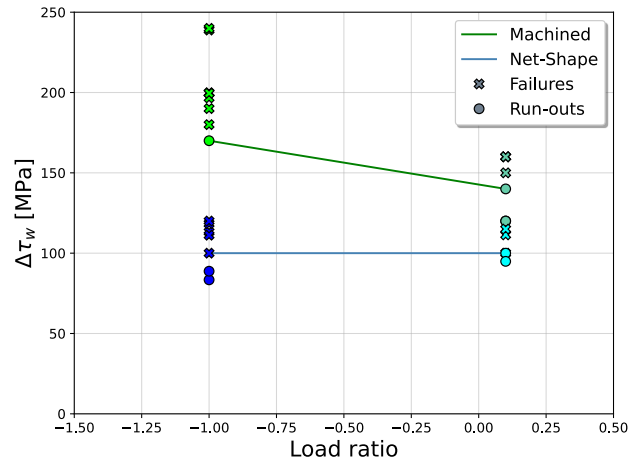
Figure 16: Comparison between the torsional fatigue strength function of load ratios for machined and net-shape specimens.

6. Conclusions

In this work, the axial and torsional fatigue behaviours of AlSi10Mg alloy were extensively analysed. The effect of machined and net-shape surface conditions were analysed considering both the killer defects as well the residual stress field in the specimens. Based on the experimental results obtained and the analysis performed, the following conclusions can be made:

1. Both machined and net-shape specimens were affected by the presence of defects. The dimension of the killer defects in the two analysed surface states, both in the case of axial and torsional loads, were found to be comparable. The main difference between the two specimen types was related to the differences in residual stresses, which were in compression for machined specimens and in tension for net-shape specimens. The residual stress field changes the effective stress ratio at which the materials are cycling, hence affecting their fatigue performances.

2. The expected dependence of torsional fatigue strength upon stress ratio for machined specimens were confirmed by the experimental results, contrarily to net-shape ones. In torsional net-shape specimens, the residual stresses in $R_T = 0.1$ tests were found to be completely released at the mid-life, because the maximum Mises stress exceeded the material's yield strength. This led to the same torsional fatigue limit for both torsional load ratios (i.e. $R_T = -1$ and $R_T = 0.1$) applied to the net-shape specimens.

3. Effective Kitagawa model in terms of SIF can be adopted to describe reasonably well the experimental results obtained from torsional fatigue testing, if the effective stress ratio is considered for expressing the material threshold $\Delta K_{\mathrm{th}} = f(\sqrt{\mathrm{area}})$.

4. The different failure mechanisms in torsion was triggered by the geometry of the killer defects, namely spherical or elongated. This also influenced the ratio between torsional and axial/bending fatigue limits. Being the ratio between torsional and axial/bending fatigue limit for the spherical defects $\Delta\tau_{\mathrm{w}}/\Delta\sigma_{\mathrm{w}} = 0.855$, this defect family represents the most critical condition for torsional fatigue if they have a size comparable to elongated defects (LOFs or surface features).

5. The results of this activity can be seen as the bases to develop a multiaxial fatigue model for AMed AlSi10Mg, taking into account the combined effects of defects and manufacturing residual stresses.

7. Acknowledgements

8. Author contributions

Contributions made to this paper are as follows: (i) F. Sausto performed part of the tests together with the analysis of the experimental results, he took care of preparing the manuscript; (ii) P. E. Carrion performed part of the tests and helped with the reviewing of the manuscript; (iii) N. Shamsaei helped with the schematization of the paper and making fully available the laboratories of NCAME for the experimental tests; (iv) S. Beretta directed this research activity with advices about the defect tolerant models used to describe the fatigue strength of AlSi10Mg, he contributed to the preparation and revision of the manuscript.

References

[1] M. Gorelik, Additive manufacturing in the context of structural integrity, International Journal of Fatigue 94 (2017) 168–177.

[2] N. Sanaei, A. Fatemi, Defects in additive manufactured metals and their effect on fatigue performance: A state-of-the-art review, Progress in Materials Science 117 (2021) 100724.

[3] A. Yadollahi, N. Shamsaei, Additive manufacturing of fatigue resistant materials: Challenges and opportunities, International Journal of Fatigue 98 (2017) 14–31.

[4] S. Beretta, S. Romano, A comparison of fatigue strength sensitivity to defects for materials manufactured by am or traditional processes, International Journal of Fatigue 94 (2017) 178–191.

[5] S. Romano, A. Brückner-Foit, A. Brandão, J. Gumpinger, T. Ghidini, S. Beretta, Fatigue properties of alsi10mg obtained by additive manufacturing: Defect-based modelling and prediction of fatigue strength, Engineering Fracture Mechanics 187 (2018) 165–189.

[6] H. Masuo, Y. Tanaka, S. Morokoshi, H. Yagura, T. Uchida, Y. Yamamoto, Y. Murakami, Effects of defects, surface roughness and hip on fatigue strength of ti-6al-4v manufactured by additive manufacturing, Procedia Structural Integrity 7 (2017) 19–26.

[7] G. Meneghetti, D. Rigon, C. Gennari, An analysis of defects influence on axial fatigue strength of maraging steel specimens produced by additive manufacturing, International journal of fatigue 118 (2019) 54–64.

[8] Y. Murakami, Metal fatigue: effects of small defects and nonmetallic inclusions, Academic Press, 2019.

[9] N. Sanaei, A. Fatemi, Defect-based fatigue life prediction of l-pbf additive manufactured metals, Engineering Fracture Mechanics 244 (2021) 107541.

[10] S. Romano, L. Patriarca, S. Foletti, S. Beretta, Lcf behaviour and a comprehensive life prediction model for alsi10mg obtained by slm, International Journal of fatigue 117 (2018) 47–62.

[11] F. Sausto, G. Marchese, E. Bassini, M. Calandri, S. Biamino, D. Ugues, S. Foletti, S. Beretta, Anisotropic mechanical and fatigue behaviour of inconel718 produced by slm in lcf and high-temperature conditions, Fatigue & Fracture of Engineering Materials & Structures 44 (1) (2021) 271–292.

[12] S. Beretta, More than 25 years of extreme value statistics for defects: Fundamentals, historical developments, recent applications, International Journal of Fatigue 151 (2021) 106407.

[13] N. Sanaei, A. Fatemi, N. Phan, Defect characteristics and analysis of their variability in metal l-pbf additive manufacturing, Materials & Design 182 (2019) 108091.

[14] Z. Wu, S. Wu, J. Bao, W. Qian, S. Karabal, W. Sun, P. J. Withers, The effect of defect population on the anisotropic fatigue resistance of alsi10mg alloy fabricated by laser powder bed fusion, International Journal of Fatigue 151 (2021) 106317.

[15] S. Romano, S. Miccoli, S. Beretta, A new fe post-processor for probabilistic fatigue assessment in the presence of defects and its application to am parts, International Journal of Fatigue 125 (2019) 324–341.

[16] F. Cabanettes, A. Joubert, G. Chardon, V. Dumas, J. Rech, C. Grosjean, Z. Dimkovski, Topography of as built surfaces generated in metal additive manufacturing: a multi scale analysis from form to roughness, Precision Engineering 52 (2018) 249–265.

[17] M. H. Nasab, S. Romano, D. Gastaldi, S. Beretta, M. Vedani, Combined effect of surface anomalies and volumetric defects on fatigue assessment of alsi7mg fabricated via laser powder bed fusion, Additive Manufacturing 34 (2020) 100918.

[18] H. Masuo, Y. Tanaka, S. Morokoshi, H. Yagura, T. Uchida, Y. Yamamoto, Y. Murakami, Influence of defects, surface roughness and hip on the fatigue strength of ti-6al-4v manufactured by additive manufacturing, International Journal of Fatigue 117 (2018) 163–179.

[19] G. Nicoletto, R. Konečná, M. Frkáň, E. Riva, Surface roughness and directional fatigue behavior of as-built ebm and dmls ti6al4v, International journal of fatigue 116 (2018) 140–148.

[20] D. Greitemeier, C. Dalle Donne, F. Syassen, J. Eufinger, T. Melz, Effect of surface roughness on fatigue performance of additive manufactured ti–6al–4v, Materials Science and Technology 32 (7) (2016) 629–634.

[21] A. Yadollahi, M. Mahtabi, A. Khalili, H. Doude, J. Newman Jr, Fatigue life prediction of additively manufactured material: Effects of surface roughness, defect size, and shape, Fatigue & Fracture of Engineering Materials & Structures 41 (7) (2018) 1602–1614.

[22] P. Nezhadfar, S. Thompson, A. Saharan, N. Phan, N. Shamsaei, Structural integrity of additively manufactured aluminum alloys: Effects of build orientation on microstructure, porosity, and fatigue behavior, Additive Manufacturing 47 (2021) 102292.

[23] M. Muhammad, P. Nezhadfar, S. Thompson, A. Saharan, N. Phan, N. Shamsaei, A comparative investigation on the microstructure and mechanical properties of additively manufactured aluminum alloys, International Journal of Fatigue 146 (2021) 106165.

[24] S. Beretta, M. Gargourimotlagh, S. Foletti, A. Du Plessis, M. Riccio, Fatigue strength assessment of "as built" alsi10mg manufactured by slm with different build orientations, International Journal of Fatigue 139 (2020) 105737.

[25] S. Romano, P. Nezhadfar, N. Shamsaei, M. Seifi, S. Beretta, High cycle fatigue behavior and life prediction for additively manufactured 17-4 ph stainless steel: Effect of sub-surface porosity and surface roughness, Theoretical and Applied Fracture Mechanics 106 (2020) 102477.

[26] P. Dong, F. Brust, Welding residual stresses and effects on fracture in pressure vessel and piping components: a millennium review and beyond, J. Pressure Vessel Technol. 122 (3) (2000) 329–338.

[27] L. Wang, X. Jiang, Y. Zhu, X. Zhu, J. Sun, B. Yan, An approach to predict the residual stress and distortion during the selective laser melting of alsi10mg parts, The International Journal of Advanced Manufacturing Technology 97 (9-12) (2018) 3535–3546.

[28] L. Parry, I. Ashcroft, R. D. Wildman, Understanding the effect of laser scan strategy on residual stress in selective laser melting through thermo-mechanical simulation, Additive Manufacturing 12 (2016) 1–15.

[29] A. Salmi, E. Atzeni, Residual stress analysis of thin alsi10mg parts produced by laser powder bed fusion, Virtual and Physical Prototyping 15 (1) (2020) 49–61.

[30] H. Ali, H. Ghadbeigi, K. Mumtaz, Effect of scanning strategies on residual stress and mechanical properties of selective laser melted ti6al4v, Materials Science and Engineering: A 712 (2018) 175–187.

[31] A. Fatemi, N. Shamsaei, Multiaxial fatigue: An overview and some approximation models for life estimation, International Journal of Fatigue 33 (8) (2011) 948–958.

[32] A. Fatemi, R. Molaei, S. Sharifimehr, N. Phan, N. Shamsaei, Multiaxial fatigue behavior of wrought and additive manufactured ti-6al-4v including surface finish effect, International Journal of Fatigue 100 (2017) 347–366.

[33] A. Fatemi, R. Molaei, S. Sharifimehr, N. Shamsaei, N. Phan, Torsional fatigue behavior of wrought and additive manufactured ti-6al-4v by powder bed fusion including surface finish effect, International Journal of Fatigue 99 (2017) 187–201.

[34] R. Molaei, A. Fatemi, N. Phan, Significance of hot isostatic pressing (hip) on multiaxial deformation and fatigue behaviors of additive manufactured ti-6al-4v including build orientation and surface roughness effects, International Journal of Fatigue 117 (2018) 352–370.

[35] R. Molaei, A. Fatemi, Crack paths in additive manufactured metallic materials subjected to multiaxial cyclic loads including surface roughness, hip, and notch effects, International Journal of Fatigue 124 (2019) 558–570.

[36] V.-D. Le, F. Morel, D. Bellett, N. Saintier, P. Osmond, Multiaxial high cycle fatigue damage mechanisms associated with the different microstructural heterogeneities of cast aluminium alloys, Materials Science and Engineering: A 649 (2016) 426–440.

[37] A. Nourian-Avval, A. Fatemi, Fatigue performance and life prediction of cast aluminum under axial, torsion, and multiaxial loadings, Theoretical and Applied Fracture Mechanics 111 (2021) 102842.

[38] R. Cryderman, N. Shamsaei, A. Fatemi, Effects of continuous cast section size on torsion deformation and fatigue of induction hardened 1050 steel shafts, Journal of Materials Processing Technology 211 (1) (2011) 66–77.

[39] A. Du Plessis, S. Beretta, Killer notches: the effect of as-built surface roughness on fatigue failure in alsi10mg produced by laser powder bed fusion, Additive Manufacturing 35 (2020) 101424.

[40] S. Beretta, Y. Murakami, Sif and threshold for small cracks at small notches under torsion, Fatigue and fracture of engineering materials and structures (2000).

[41] M. Endo, The multiaxial fatigue strength of specimens containing small defects, in: European structural integrity society, Vol. 31, Elsevier, 2003, pp. 243–264.

[42] M. Endo, A. McEvily, Fatigue crack growth from small defects under out-of-phase combined loading, Engineering fracture mechanics 78 (8) (2011) 1529–1541.

[43] Y. Murakami, K. Takahashi, Torsional fatigue of a medium carbon steel containing an initial small surface crack introduced by tension-compression fatigue: crack branching, non-propagation and fatigue limit, Fatigue & fracture of engineering materials & structures (Print) 21 (12) (1998) 1473–1484.

[44] S. Beretta, S. Foletti, K. Valiullin, Fatigue strength for small shallow defects/cracks in torsion, International journal of fatigue 33 (3) (2011) 287–299.

[45] M. Endo, K. Yanase, Crack path and threshold condition for small fatigue crack growth in annealed carbon steels under fully-reversed torsional loading, International Journal of Fatigue 125 (2019) 112–121.

[46] G. Sines, Behavior of metals under complex static and alternating stresses, Metal fatigue 1 (1959) 145–169.

[47] P. Davoli, A. Bernasconi, M. Filippini, S. Foletti, I. Papadopoulos, Independence of the torsional fatigue limit upon a mean shear stress, International journal of fatigue 25 (6) (2003) 471–480.

[48] S. Lee, B. Rasoolian, D. F. Silva, J. W. Pegues, N. Shamsaei, Surface roughness parameter and modeling for fatigue behavior of additive manufactured parts: A non-destructive data-driven approach, Additive Manufacturing 46 (2021) 102094.

[49] ISO, Geometrical Product Specifications (GPS) - Surface texture: Profile method - Terms, definitions and surface texture parameters, Standard, International Organization for Standardization (1997).

[50] ISO, Geometrical Product Specifications (GPS)- Surface texture: Profile method- Rules and procedures for the assessment of surface texture, Standard, International Organization for Standardization (1998).

[51] J. Seewig, P. Scott, M. Eifler, B. Barwick, D. Hüser, Crossing-the-line segmentation as a basis for rsm and rc evaluation, Surface Topography: Metrology and Properties 8 (2) (2020) 024010.

[52] ISO, Standards Publication Metallic materials - Torque controlled fatigue testing, standard, International Organization for Standardization (2011).

[53] B. S. Institution, Metallic Materials. Tensile Testing: Method of Test at Room Temperature, British Standards Institution, 2020.

[54] ASTM, Standard test method for strain-controlled fatigue testing, ASTM Standard E606 (2012).

[55] ASTM, Standard Practice for Statistical Analysis of Linear or Linearized Stress-Life (S-N) and Strain-Life (ε-N) Fatigue Data, American Society for Testing and Materials (2010).

[56] K. Brownlee, J. Hodges Jr, M. Rosenblatt, The up-and-down method with small samples, Journal of the American Statistical Association 48 (262) (1953) 262–277.

[57] Y. Murakami, Quantitative evaluation of effect of surface roughness on fatigue strength, JSME 62 (1996) 1124.

[58] S. Beretta, Affidabilità delle costruzioni meccaniche: Strumenti e metodi per l'affidabilità di un progetto, Springer Science & Business Media, 2010.

[59] M. Endo, Y. Murakami, Effects of an artificial small defect on torsional fatigue strength of steels, The american society of mechanical engineers (1987).

[60] T. M. M. Shiratori, Stress Intensity Factors Handbook, Vol. 2, Soc. Mater. Sci., Japan, 1985.

[61] Y. Murakami, Analysis of stress intensity factors of modes i, ii and iii for inclined surface cracks of arbitrary shape, Engineering Fracture Mechanics 22 (1) (1985) 101–114.

[62] Y. Murakami, S. Nemat-Nasser, Growth and stability of interacting surface flaws of arbitrary shape, Engineering Fracture Mechanics 17 (3) (1983) 193–210.

[63] F. Erdogan, G. Sih, On the crack extension in plates under plane loading and transverse shear, The american society of mechanical engineers (1963).

[64] M. Kassir, G. C. Sih, Three-dimensional stress distribution around an elliptical crack under arbitrary loadings, The american society of mechanical engineers (1966).

[65] A. Yadollahi, N. Shamsaei, S. M. Thompson, A. Elwany, L. Bian, Effects of building orientation and heat treatment on fatigue behavior of selective laser melted 17-4 ph stainless steel, International Journal of Fatigue 94 (2017) 218–235.

[66] M. El Haddad, T. Topper, K. Smith, Prediction of non propagating cracks, Engineering fracture mechanics 11 (3) (1979) 573–584.

[67] K. Miller, The short crack problem, Fatigue & Fracture of Engineering Materials & Structures 5 (3) (1982) 223–232.

755 [68] S. Beretta, L. Patriarca, M. Gargourimotlagh, A. Hardaker, D. Brackett, M. Salimian, J. Gumpinger, T. Ghidini, A benchmark activity on the fatigue life assessment of alsi10mg components manufactured by l-pbf, Accepted by Materials & Design (2021).

[69] N. E. Dowling, Mechanical Behavior of Materials: Engineering Methods for Deformation, Fracture, and Fatigue, fourth edition, Pearson Higher Ed, 2013.

Appendix A. Fatigue results of machined specimens

The following table reports all the data related to fatigue tests of machined specimens.

Table A.8: Test results of the machined specimens.

Test type	$\Delta\sigma$ [MPa]	$\Delta\tau$ [MPa]	Load ratio [-]	N_f [cycles]	$\sqrt{\text{area}}$ [µm]	h/r [-]	Defect type
Axial	357.46		-1	9648	86	1.58	Pore
Axial	355.13		-1	9219	119	0.57	LoF
Axial	305.51		-1	99 957	83	1.29	Pore
Axial	299.74		-1	29 002	173	0.79	LoF
Axial	292.72		-1	157 527	85	1.60	Pore
Axial	256.02		-1	119 042	84	1.06	Pore
Axial	247.48		-1	227 604	79	1.66	Pore
Axial	241.26		-1	1 122 736	73	0.89	Pore
Axial	230.84		-1	76 704	112	2.35	LoF
Axial	204.81		-1	314 622	208	0.61	LoF
Axial	203.58		-1	5 000 000	83	1.29	Pore
Axial	194.63		-1	5 000 000	84	1.06	Pore
Torsional		319.92	-1	4302	NA[1]	NA[1]	
Torsional		280.00	-1	9369	NA[1]	NA[1]	
Torsional		277.75	-1	23 730	NA[1]	NA[1]	
Torsional		269.70	-1	4917	NA[1]	NA[1]	
Torsional		239.94	-1	118 288	88	1.09	Pore
Torsional		238.88	-1	92 358	59	0.80	Pore
Torsional		199.89	-1	124 975	146	0.91	LoF
Torsional		196.67	-1	525 040	71	1.57	Pore
Torsional		190.00	-1	242 371	152	0.34	LoF
Torsional		180.01	-1	1 497 325	63	1.42	Pore
Torsional		170.00	-1	5 000 000	152	0.34	LoF
Torsional		199.98	0.1	65 925	75	1.06	LoF
Torsional		199.84	0.1	76 861	57	1.77	LoF
Torsional		199.65	0.1	69 385	86	0.82	Pore
Torsional		159.75	0.1	308 366	57	0.73	Pore
Torsional		159.57	0.1	507 182	66	1.46	LoF
Torsional		159.51	0.1	284 309	86	0.90	Pore
Torsional		149.50	0.1	1 995 348	61	1.47	Pore
Torsional		139.25	0.1	10 000 000	61	1.47	Pore
Torsional		119.76	0.1	5 086 538	86	0.90	Pore
Torsional		119.75	0.1	10 182 396	57	1.77	LoF

---

[1]These specimens failed due to shear cracks due to the elevated applied load. At the end of the tests the fracture surfaces were too much damaged to be analysed.

Appendix B. Fatigue results of net-shape specimens

The following table reports all the data related to fatigue tests of net-shape specimens.

Table B.9: Test results of the net-shape specimens.

Test type	$\Delta\sigma$ [MPa]	$\Delta\tau$ [MPa]	Load ratio [-]	N_f [cycles]	w [µm]	t [µm]	$\sqrt{\text{area}}$ [µm]	Defect type
Axial	197.77		-1	55 864	379	43	110	Superficial feature
Axial	178.02		-1	44 670	408	81	119	Spherical powder particles
Axial	173.46		-1	87 333	241	38	86	Superficial feature
Axial	169.24		-1	80 534	213	46	120	Superficial feature
Axial	139.58		-1	193 891	602	38	119	Superficial feature
Axial	137.67		-1	195 046	380	85	117	Spherical powder particles
Axial	133.44		-1	172 806	129	89	93	Spherical powder particles
Axial	126.87		-1	215 048	404	69	108	Spherical powder particles
Axial	116.74		-1	247 921	810	58	183	Superficial feature
Axial	112.81		-1	350 854	349	40	100	Superficial feature
Axial	111.99		-1	254 929	725	49	154	Superficial feature
Axial	102.04		-1	513 691	391	39	122	Superficial feature
Axial	95.28		-1	5 000 000	129	89	93	Spherical powder particles
Axial	81.40		-1	5 000 000	404	69	108	Spherical powder particles
Torsional		180.00	-1	143 500	130	59	77	Spherical powder particles
Torsional		180.00	-1	143 500	166	50	79	Spherical powder particles
Torsional		180.00	-1	143 500	199	60	89	Spherical powder particles
Torsional		180.00	-1	121 300	670	124	256	Superficial feature
Torsional		160.00	-1	258 900	246	64	91	Superficial feature
Torsional		157.18	-1	210 900	132	73	86	Spherical powder particles
Torsional		139.93	-1	363 500	389	41	98	Superficial feature
Torsional		139.89	-1	291 700	220	98	108	Superficial feature
Torsional		120.00	-1	1 198 800	248	127	125	Superficial feature
Torsional		118.37	-1	674 400	285	60	109	Superficial feature
Torsional		113.26	-1	1 151 800	501	48	152	Superficial feature
Torsional		111.18	-1	510 500	437	79	119	Spherical powder particles
Torsional		100.00	-1	2 039 500	423	30	96	Superficial feature
Torsional		88.77	-1	5 000 000	285	60	109	Superficial feature
Torsional		83.39	-1	5 000 000	437	79	119	Spherical powder particles
Torsional		159.42	0.1	163 800	234	34	80	Spherical powder particles
Torsional		159.42	0.1	152 800	99	48	59	Spherical powder particles
Torsional		140.00	0.1	298 200	387	47	116	Superficial feature
Torsional		130.00	0.1	390 500	148	81	81	Spherical powder particles
Torsional		120.00	0.1	443 300	180	52	80	Spherical powder particles
Torsional		119.89	0.1	586 900	315	88	121	Superficial feature
Torsional		115.00	0.1	477 300	141	49	63	Spherical powder particles
Torsional		111.39	0.1	906 800	340	81	128	Superficial feature
Torsional		100.00	0.1	5 000 000	99	48	59	Spherical powder particles
Torsional		100.00	0.1	1 190 900	224	63	92	Spherical powder particles
Torsional		94.91	0.1	10 000 000	315	88	121	Superficial feature

Appendix C. XRD measurements of residual stresses

Table C.10: Results of the residual stresses measurements on the two torsional specimens. Indexes *A* and *B* are referred to the two opposing specimen's surfaces. Θ is the angle between the measuring direction and the specimen's long axis. For each measured value of the stress it is also reported the deviation and the Full With at Half Maximum (FWHM) with the corresponding deviation.

Position	Depth [µm]	Θ = 0° Stress [MPa]	Deviation [MPa]	FWHM [°]	Deviation [°]	Θ = 45° Stress [MPa]	Deviation [MPa]	FWHM [°]	Deviation [°]	Θ = 90° Stress [MPa]	Deviation [MPa]	FWHM [°]	Deviation [°]
						Specimen F13							
A	0.0	141.5	16.8	1.44	0.17	80.0	14.6	1.45	0.10	95.0	13.2	1.49	0.14
A	55.0	85.1	21.2	1.38	0.12	75.7	13.2	1.41	0.14	79.6	19.7	1.47	0.15
A	100.7	135.7	18.4	1.37	0.14	104.0	13.5	1.36	0.11	94.7	17.8	1.44	0.20
A	542.7	123.0	7.6	1.46	0.17	64.0	8.7	1.45	0.14	22.5	6.9	1.45	0.14
B	0.0	77.1	16.9	1.39	0.11	36.0	16.0	1.44	0.16	18.5	13.1	1.43	0.09
B	53.0	96.8	17.9	1.36	0.12	72.3	20.1	1.4	0.13	63.6	16.5	1.42	0.15
B	106.9	67.9	17.3	1.35	0.09	64.0	15.9	1.39	0.15	66.3	11.2	1.44	0.16
B	477.0	108.9	13.0	1.44	0.16	66.1	13.3	1.48	0.21	36.4	10.1	1.50	0.24
						Specimen P03							
A	0.0	79.2	12.5	1.42	0.12	41.4	12.8	1.43	0.13	8.2	9.8	1.43	0.12
A	53.9	91.9	12.3	1.35	0.08	54.1	17.2	1.36	0.09	91.2	16.8	1.45	0.21
A	103.1	93.1	18.6	1.35	0.14	111.7	14.5	1.38	0.12	64.1	13.9	1.43	0.19
A	552.0	125.3	6.4	1.39	0.11	89.9	8.9	1.44	0.14	41.9	12.2	1.47	0.16
B	0.0	56.7	18.0	1.44	0.11	66.3	14.1	1.42	0.14	15.6	11.1	1.45	0.15
B	45.7	37.7	24.2	1.40	0.16	63.2	11.3	1.47	0.13	50.3	15.1	1.47	0.19
B	97.8	74.8	17.1	1.35	0.11	85.1	12.7	1.40	0.13	57.6	12.4	1.45	0.19
B	655.6	156.6	9.0	1.41	0.11	95.0	6.5	1.42	0.13	85.5	5.5	1.48	0.15

Table C.11: Results of the residual stresses measurements on three axial specimens. Indexes *A*, *B* and *C* are referred to the three measures along the gauge section equispaced of 120° each. Θ is the angle between the measuring direction and the specimen's long axis. For each measured value of the stress it is also reported the deviation and the Full With at Half Maximum (FWHM) with the corresponding deviation.

Position	Depth [µm]	Θ = 0° Stress [MPa]	Deviation [MPa]	FWHM [°]	Deviation [°]	Θ = 90° Stress [MPa]	Deviation [MPa]	FWHM [°]	Deviation [°]
			Specimen B 15 - machined						
A	0.0	-92.7	6.4	1.54	0.11	-93.5	5.9	1.48	0.08
A	63.5	3.7	7.9	1.41	0.12	-27.7	7.9	1.37	0.09
A	104.0	71.9	5.4	1.40	0.10	19.5	4.8	1.41	0.12
B	0.0	-57.8	4.3	1.50	0.10	-53.3	6.9	1.45	0.08
B	51.4	-12.2	7.6	1.39	0.12	-33.6	9.3	1.34	0.09
B	99.3	-13.0	6.6	1.40	0.12	-7.2	9.8	1.36	0.10
C	0.0	-87.2	3.2	1.54	0.10	-67.7	8.0	1.49	0.10
C	57.2	-44.4	7.7	1.41	0.11	-40.2	8.8	1.37	0.09
C	105.0	-37.9	7.9	1.41	0.10	-37.4	8.6	1.38	0.09
			Specimen G 15 - net-shape						
A	0.0	96.4	11.2	1.39	0.14	59.8	14.2	1.44	0.13
A	50.0	68.0	16.9	1.38	0.14	37.0	11.7	1.40	0.15
A	93.0	148.9	17.1	1.37	0.10	52.7	9.9	1.41	0.11
B	0.0	68.5	10.3	1.42	0.14	6.5	7.4	1.42	0.12
B	56.0	116.7	23.4	1.32	0.10	54.6	14.7	1.43	0.13
B	109.5	103.0	20.9	1.38	0.09	47.1	11.8	1.43	0.14
C	0.0	20.7	15.0	1.40	0.13	-6.4	9.6	1.39	0.09
C	56.0	43.4	17.9	1.33	0.11	42.1	9.0	1.41	0.14
C	94.0	90.5	18.1	1.35	0.14	59.8	9.6	1.40	0.14
			Specimen G 16 - net-shape						
A	0.0	37.3	11.2	1.42	0.12	41.3	11.9	1.43	0.11
A	57.2	0.8	29.2	1.41	0.15	18.5	15.4	1.39	0.12
A	110.8	56.8	23.0	1.39	0.16	32.9	12.9	1.42	0.13
A	364.0	109.9	18.4	1.39	0.13	49.3	11.4	1.40	0.17
A	516.8	82.2	4.9	1.44	0.14	26.9	7.4	1.43	0.14
B	0.0	54.5	15.4	1.40	0.09	29.2	9.7	1.43	0.12
B	51.2	94.5	20.2	1.38	0.12	85.4	12.7	1.42	0.11
B	94.8	75.5	18.0	1.40	0.12	55.6	13.8	1.40	0.12
B	245.0	127.9	9.5	1.43	0.14	110.3	10.0	1.52	0.22
B	509.5	128.1	8.4	1.42	0.13	27.9	7.3	1.44	0.14
C	0.0	67.7	11.7	1.44	0.14	19.4	11.8	1.44	0.12
C	45.5	66.2	9.2	1.40	0.12	60.0	10.0	1.40	0.09
C	90.5	77.7	12.6	1.36	0.08	46.8	15.6	1.42	0.10
C	255.5	132.5	11.8	1.40	0.14	51.7	12.1	1.43	0.14
C	506.8	127.2	5.1	1.46	0.15	41.1	6.0	1.44	0.14

Table C.12: Results of the XRD measurements on the torsional specimen L01 before and after testing to evaluate the residual stresses relaxation. Indexes *A*, *B*, *C* and *D* are referred to the four measurements along the gauge section equispaced 90° each. Θ is the angle between the measuring direction and the specimen's long axis. For each measured value of the stress it is also reported the deviation and the Full With at Half Maximum (FWHM) with the corresponding deviation.

		Θ = 0°				Θ = 90°			
Position	Depth [μm]	Stress [MPa]	Deviation [MPa]	FWHM [°]	Deviation [°]	Stress [MPa]	Deviation [MPa]	FWHM [°]	Deviation [°]
				Specimen L 01 - net-shape untested					
A	69.3	80.1	12.3	1.38	0.11	43.9	15.4	1.48	0.17
B	60.9	80.0	18.4	1.41	0.15	53.5	12.0	1.45	0.15
C	49.5	79.9	11.9	1.35	0.10	67.0	14.6	1.43	0.17
D	62.1	80.7	18.5	1.36	0.11	66.1	13.9	1.44	0.16
				Specimen L 01 - net-shape tested					
A	69.3	1.0	13.2	1.39	0.11	27.7	9.0	1.43	0.16
B	60.9	16.3	16.4	1.41	0.14	23.5	12.0	1.43	0.14
C	49.5	-3.2	10.5	1.40	0.13	33.6	8.6	1.42	0.17
D	62.1	-8.1	17.4	1.37	0.13	47.8	12.3	1.43	0.15